The ALMA Survey of 70 mu m Dark High-mass Clumps in Early Stages (ASHES). IX. Physical Properties and Spatial Distribution of Cores in

The Astrophysical Journal, 950:148 (18pp), 2023 June 20 https://doi.org/10.3847/1538-4357/acccea

The ALMA Survey of 70 μm Dark High-mass Clumps in Early Stages (ASHES). IX. Physical Properties and Spatial Distribution of Cores in IRDCs

Kaho Morii[1,2], Patricio Sanhueza[2,3], Fumitaka Nakamura[1,2,3], Qizhou Zhang[4], Giovanni Sabatini[5,6], Henrik Beuther[7], Xing Lu[8], Shanghuo Li[7], Guido Garay[9], James M. Jackson[10], Fernando A. Olguin[11], Daniel Tafoya[12], Ken'ichi Tatematsu[2,3], Natsuko Izumi[13], Takeshi Sakai[14], and Andrea Silva[2]
[1] Department of Astronomy, Graduate School of Science, The University of Tokyo, 7-3-1 Hongo, Bunkyo-ku, Tokyo 113-0033, Japan; kaho.morii@grad.nao.ac.jp
[2] National Astronomical Observatory of Japan, National Institutes of Natural Sciences, 2-21-1 Osawa, Mitaka, Tokyo 181-8588, Japan
[3] Astronomical Science Program, The Graduate University for Advanced Studies, SOKENDAI, 2-21-1 Osawa, Mitaka, Tokyo 181-8588, Japan
[4] Center for Astrophysics | Harvard & Smithsonian, 60 Garden Street, Cambridge, MA 02138, USA
[5] INAF—Istituto di Radioastronomia—Italian node of the ALMA Regional Centre (It-ARC), Via Gobetti 101, I-40129 Bologna, Italy
[6] INAF, Osservatorio Astrofisico di Arcetri, Largo E. Fermi 5, I-50125 Firenze, Italy
[7] Max Planck Institute for Astronomy, Konigstuhl 17, D-69117 Heidelberg, Germany
[8] Shanghai Astronomical Observatory, Chinese Academy of Sciences, 80 Nandan Road, Shanghai 200030, People's Republic of China
[9] Departamento de Astronomía, Universidad de Chile, Las Condes, Santiago 7550000, Chile
[10] Green Bank Observatory, 155 Observatory Rd, Green Bank, WV 24944, USA
[11] Institute of Astronomy and Department of physics, National Tsing Hua University, Hsinchu 30013, Taiwan
[12] Department of Space, Earth and Environment, Chalmers University of Technology, Onsala Space Observatory, SE-439 92 Onsala, Sweden
[13] Academia Sinica Institute of Astronomy and Astrophysics, 11F of AS/NTU Astronomy-Mathematics Building, No.1, Section 4, Roosevelt Road, Taipei 10617, Taiwan
[14] Graduate School of Informatics and Engineering, The University of Electro-Communications, Chofu, Tokyo 182-8585, Japan
Received 2022 December 22; revised 2023 April 1; accepted 2023 April 4; published 2023 June 20

Abstract

The initial conditions found in infrared dark clouds (IRDCs) provide insights on how high-mass stars and stellar clusters form. We have conducted high-angular resolution and high-sensitivity observations toward thirty-nine massive IRDC clumps, which have been mosaicked using the 12 and 7 m arrays from the Atacama Large Millimeter/submillimeter Array. The targets are 70 μm dark massive (220–4900 $M_\odot$), dense (>10^4 cm^{-3}), and cold (~10–20 K) clumps located at distances between 2 and 6 kpc. We identify an unprecedented number of 839 cores, with masses between 0.05 and 81 $M_\odot$ using 1.3 mm dust continuum emission. About 55% of the cores are low-mass (<1 $M_\odot$), whereas $\lesssim$1% (7/839) are high-mass ($\gtrsim$27 $M_\odot$). We detect no high-mass prestellar cores. The most massive cores (MMC) identified within individual clumps lack sufficient mass to form high-mass stars without additional mass feeding. We find that the mass of the MMCs is correlated with the clump surface density, implying denser clumps produce more massive cores. There is no significant mass segregation except for a few tentative detections. In contrast, most clumps show segregation once the clump density is considered instead of mass. Although the dust continuum emission resolves clumps in a network of filaments, some of which consist of hub-filament systems, the majority of the MMCs are not found in the hubs. Our analysis shows that high-mass cores and MMCs have no preferred location with respect to low-mass cores at the earliest stages of high-mass star formation.

Unified Astronomy Thesaurus concepts: Infrared dark clouds (787); Star formation (1569); Star forming regions (1565); Protoclusters (1297); Protostars (1302)

Supporting material: figure sets, machine-readable tables

1. Introduction

The study of cores embedded in massive prestellar clumps is expected to provide important information on the early phases of high-mass stars >8 $M_\odot$ and cluster formation. For instance, the spatial distribution of cores, the fragmentation properties, and core masses would help to understand the very early phase of star formation from the clump to core scale. Do high-mass cores (e.g., $\gtrsim$30 $M_\odot$) form in the early phase, or do only low-mass cores form at early times? Is there any primordial mass segregation? Answers to these questions are important to constrain high-mass star formation scenarios.

A long debate of core accretion (e.g., McKee & Tan 2002, 2003) versus competitive accretion (e.g., Bonnell et al. 2001, 2004) has not been settled over 20 years (e.g., Tan et al. 2014). Recently, more scenarios have been proposed, such as the global hierarchical collapse (Vázquez-Semadeni et al. 2019) and the inertial-inflow model (Padoan et al. 2020; Pelkonen et al. 2021). Hub-filaments, sites where multiple filaments converge, have also attracted attention as the birthplace of high-mass stars (Myers 2009; Peretto et al. 2014; Kumar et al. 2020). The turbulent core accretion model predicts a massive core as an initial condition in which a high-mass star forms via monolithic collapse. Other models (clump-fed scenarios) predict continuous mass feeding toward initially low-mass cores that eventually accrete sufficient mass to form high-mass stars. The competitive accretion (Bonnell et al. 2001) and the global hierarchical collapse (Vázquez-Semadeni et al. 2019) models describe core growth in a cluster

environment. A cloud fragments into cores with a mass near the thermal Jeans mass, forming an initial cluster of low-mass (proto-)stars. They grow in mass by additional mass feeding. In particular, the protostars near the center of the cluster, or at the bottom of the gravitational potential, efficiently gain mass and have the largest probability of forming high-mass stars. Simulations made by Wang et al. (2010) suggest that not even the presence of magnetic fields can prevent mass accretion or core mass growth. The inertial-inflow model proposed by Padoan et al. (2020) explains the process of acquiring additional mass from converging flows.

To study the initial conditions of high-mass star formation, infrared dark clouds (IRDCs) are considered to be the best targets (Rathborne et al. 2006; Chambers et al. 2009; Sanhueza et al. 2012, 2019). They are identified by Spitzer and Herschel surveys such as the Galactic Legacy Infrared Mid-Plane Survey Extraordinaire (GLIMPSE; Benjamin et al. 2003), the survey of the inner Galactic plane using the Multiband Infrared Photometer for Spitzer (MIPSGAL; Carey et al. 2009), and the Herschel Infrared GALactic plane survey (Hi-GAL; Molinari et al. 2010), and studied in millimeter and submillimeter surveys such as the Atacama Pathfinder Experiment Telescope Large Area Survey of the Galaxy (ATLASGAL; Schuller et al. 2009), the Bolocam Galactic Plane Survey (BGPS; Aguirre et al. 2011), the millimeter Astronomy Legacy Team 90 GHz (MALT90) survey (Foster et al. 2011, 2013; Jackson et al. 2013), and the Radio Ammonia Mid-plane Survey (RAMPS, Hogge et al. 2018). Recent observations, using sub/millimeter arrays such as Submillimeter Array (SMA), Combined Array for Research in Millimeter-wave Astronomy (CARMA), Northern Extended Millimeter Array, and Atacama Large Millimeter/submillimeter Array (ALMA), have achieved high spatial resolution and high sensitivity, resolving dense cores embedded in IRDCs even though they are at far distances from the Sun (over a few kiloparsecs). Most case studies have investigated which physical processes affect the fragmentation (e.g., Zhang et al. 2009; Wang et al. 2011; Zhang et al. 2014; Ohashi et al. 2016; Csengeri et al. 2017; Li et al. 2019; Sanhueza et al. 2019; Li et al. 2021; Liu et al. 2022; Zhang et al. 2021), whether high-mass prestellar cores exist (e.g., Zhang & Wang 2011; Lu et al. 2015; Sanhueza et al. 2017; Louvet et al. 2019; Pillai et al. 2019; Svoboda et al. 2019; Barnes et al. 2021), if low-mass cores form before, coevally, or after the formation of high-mass cores (e.g., Zhang et al. 2015; Pillai et al. 2019; Svoboda et al. 2019; Li et al. 2021), if cores acquire additional mass from their surroundings (Schneider et al. 2010; Henshaw et al. 2014; Contreras et al. 2018; Olguin et al. 2021; Redaelli et al. 2022), and their chemistry (Sanhueza et al. 2012, 2013; Sakai et al. 2015, 2018; Feng et al. 2020; Liu et al. 2020; Sabatini et al. 2022; Sakai et al. 2022), for example. However, the small sample size and possible environmental effects make it difficult to reach general conclusions. A systematic study of a statistically significant sample of IRDCs is desired to characterize the core properties, especially in the very early prestellar phase.

We have conducted the ALMA Survey of 70 μm Dark High-mass Clumps in Early Stages (ASHES). The angular resolution of $\sim 1\farcs2$ allowed us to resolve cores embedded in clumps. In a pilot survey, we mosaicked twelve candidate massive prestellar clumps with ALMA in dust continuum and molecular line emission at $\sim$224 GHz (Sanhueza et al. 2019). We investigated fragmentation process (Sanhueza et al. 2019), outflows (Li et al. 2020), chemistry (Li et al. 2022; Sabatini et al. 2022), and dynamical properties (Li et al. 2023). We also conducted some case studies about a peculiar outflow (Tafoya et al. 2021), active star formation signatures (Morii et al. 2021), and deuterated chemistry (Sakai et al. 2022).

Here, we present the dust continuum emission of the complete sample toward thirty-nine targets, and study core physical properties such as core mass and spatial distribution, and, in particular, the properties of the most massive cores (MMCs) in each clump. The paper is organized as follows: Section 2 describes the sample selection. Section 3 summarizes the observation setups and data analysis. Results are presented in Section 4, and we discuss core mass, a correlation between the mass and the spatial distribution of the MMCs in Sections 5.1 and 5.2, respectively. Finally, we discuss the high-mass star formation picture based on our finding in Sections 5.3, and Section 6 concludes the present study.

2. Sample Selection

2.1. Selection Strategy

We selected massive prestellar clump candidates without bright infrared sources to reveal the very early phase of high-mass star formation from the first and fourth quadrants following Traficante et al. (2015) and the MALT90 survey (Foster et al. 2011, 2013; Jackson et al. 2013), respectively. In the MALT90 survey, Jackson et al. (2013) used the ATLASGAL 870 μm survey to select a sample of 3246 high-mass clumps, almost all in the fourth quadrant, that were observed in molecular lines. Combining Herschel and ATLASGAL dust continuum emission, Guzmán et al. (2015) derived column density and dust temperature maps for the whole sample. Whitaker et al. (2017) derived kinematic distances, and Contreras et al. (2017) calculated the mass, density, and luminosities of the clumps. Guzmán et al. (2015) classified clumps that lack from 3.6 to 70 μm (Spitzer/Herschel) compact emission as quiescent, which are the best prestellar clump candidates.

The mean temperature of these clumps is $\sim$15 K, with a range from 9 to 23 K, supporting the idea that these clumps host the early stages of star formation. We impose additional selection criteria for clump mass and density to ensure the selection of the best prestellar candidates with the potential to form high-mass stars. The clump mass, the mass surface density, and the volume density should be larger than 500 $M_\odot$, $\sim$0.1 g cm^{-2}, and 5×10^3 cm^{-3}, respectively. In addition, targets are limited to within a distance of 6 kpc to ensure good spatial resolutions. At this distance, the angular resolution is comparable to the size of low-mass cores (Kirk et al. 2006, e.g., $\sim$7000 au). For some clumps that are not included in the analysis of Contreras et al. (2017),[15] we estimate clump mass by using the column density and radius from Guzmán et al. (2015) and the distance from Whitaker et al. (2017). Finally, we selected 18 clumps only in the fourth quadrant satisfying the conditions above, from which 11 were presented in the pilot survey (Sanhueza et al. 2019).

We selected additional sources from the first quadrant, using the work by Traficante et al. (2015), who studied 3493 clumps using dust emission from Herschel and ^{13}CO ($J = 1 - 0$) emission from the Galactic Ring Survey Jackson06, and identified 667 starless clump candidates with no counterpart

[15] Clumps not included in Contreras et al. (2017) are G010.991–00.082, G014.492–00.139, G331.372–00.116, G333.481–00.224, G340.222–00.167, and G340.232–00.146.

Table 1
Physical Properties of ASHES Clumps

Clump Name	R.A. (ICRS)	Decl. (ICRS)	σ (km s^{-1})	d (kpc)	T_{cl} (K)	M_{ref} ($M_\odot$)	R_{cl} (pc)	M_{cl} ($M_\odot$)	Σ_{cl} (g cm^{-2})	$n(H_2)_{cl}$ (10^4 cm^{-3})
(1)	(2)	(3)	(4)	(5)	(6)	(7)	(8)	(9)	(10)	(11)
G010.991–00.082	18:10:06.65	−19:27:50.7	1.1	3.7	12.0	2230	0.49	2300	0.64	6.74
G014.492–00.139	18:17:22.03	−16:25:01.9	1.8	3.9	13.0	5200	0.44	3200	1.11	13.30
G015.203–00.441	18:19:52.56	−15:56:00.2	1.0	2.4	20.1	930	0.27	400	0.33	7.14
G016.974–00.222	18:22:31.99	−14:16:02.3	1.2	3.6	12.8	1378	0.26	200	0.21	4.02
G018.801–00.297	18:26:19.27	−12:41:17.3	1.3	4.7	13.3	2809	0.72	4500	0.57	4.08
G018.931–00.029	18:25:35.70	−12:26:53.7	1.5	3.6	20.7	423	0.76	2500	0.30	2.00
G022.253+00.032	18:31:39.60	−09:28:39.5	1.0	5.2	13.8	3010	0.32	400	0.24	4.29
G022.692–00.452	18:34:13.78	−09:18:42.2	1.2	4.9	18.0	1426	0.39	300	0.13	1.70
G023.477+00.114	18:33:39.53	−08:21:09.6	1.3	5.3	13.9	1000	0.38	1300	0.61	8.48
G024.010+00.489	18:33:18.40	−07:42:28.1	1.0	5.7	12.7	3529	0.26	600	0.57	11.97
G024.524–00.139	18:36:30.82	−07:32:26.6	1.5	5.5	13.1	1555	0.76	3700	0.43	2.89
G025.163–00.304	18:38:17.20	−07:02:58.3	1.2	4.2	12.9	7245	0.46	1100	0.33	3.84
G028.273–00.167	18:43:31.32	−04:13:19.5	1.6	5.0	10.9	1722	0.47	1700	0.50	5.71
G028.541–00.237	18:44:15.80	−04:00:49.8	1.4	5.3	13.9	6028	0.63	2100	0.35	2.91
G028.564–00.236	18:44:18.09	−03:59:33.5	1.9	5.3	12.7	15276	0.59	4900	0.94	8.43
G028.927+00.394	18:42:43.18	−03:22:56.3	1.0	5.9	15.4	1616	0.46	700	0.22	2.45
G030.704+00.104	18:47:00.12	−01:56:03.9	1.5	5.9	15.0	1749	0.76	2200	0.25	1.76
G030.913+00.719	18:45:11.58	−01:28:08.2	0.9	3.5	12.4	1074	0.27	400	0.32	7.00
G033.331–00.531	18:54:03.20	+00:06:53.4	2.0	6.1	14.3	1065	0.57	600	0.13	1.13
G034.133+00.076	18:53:21.47	+01:06:12.1	1.2	3.8	16.0	579	0.55	700	0.17	1.49
G034.169+00.089	18:53:22.57	+01:08:29.7	1.0	3.8	17.9	596	0.38	300	0.14	1.83
G034.739–00.119	18:55:09.83	+01:33:14.5	1.2	5.3	12.7	2833	0.37	700	0.32	4.69
G036.666–00.114	18:58:39.77	+03:16:16.5	0.9	3.6	13.4	881	0.26	300	0.25	6.00
G305.794–00.096	13:16:33.40	−62:49:42.1	1.3	5.0	16.0	1560	0.32	900	0.58	9.06
G327.116–00.294	15:50:57.18	−54:30:33.6	1.4	3.9	14.3	580	0.39	700	0.30	4.23
G331.372–00.116	16:11:34.10	−51:35:00.1	1.8	5.4	14.0	1640	0.63	1500	0.25	2.07
G332.969–00.029	16:18:31.61	−50:25:03.1	1.1	4.3	12.6	1170	0.59	1100	0.22	1.88
G333.016–00.751	16:21:56.39	−50:53:45.2	2.1	3.7	17.6	690	0.37	300	0.15	2.12
G333.481–00.224	16:21:39.97	−50:11:44.8	1.2	3.5	18.9	593	0.31	400	0.24	4.52
G333.524–00.269	16:22:03.39	−50:11:47.2	1.5	3.5	21.2	2400	0.30	900	0.64	11.10
G337.342–00.119	16:37:21.00	−47:19:25.3	2.8	4.7	14.5	460	0.41	300	0.12	1.52
G337.541–00.082	16:37:58.48	−47:09:05.1	1.1	4.0	12.0	1180	0.42	1200	0.46	5.49
G340.179–00.242	16:48:40.88	−45:16:01.1	1.9	4.1	14.0	1470	0.74	1900	0.23	1.60
G340.222–00.167	16:48:30.83	−45:11:05.8	1.0	4.0	15.0	760	0.36	600	0.29	4.39
G340.232–00.146	16:48:27.56	−45:09:51.9	2.1	3.9	14.0	710	0.47	900	0.26	2.97
G340.398–00.396	16:50:08.85	−45:11:47.9	1.8	3.7	13.5	1690	0.64	2200	0.36	2.86
G341.039–00.114	16:51:14.11	−44:31:27.2	1.1	3.6	14.3	1070	0.47	900	0.28	3.05
G343.489–00.416	17:01:01.19	−42:48:11.0	1.0	2.9	10.3	810	0.41	800	0.32	3.98
G345.114–00.199	17:05:26.26	−41:22:55.4	1.1	2.9	11.2	1350	0.24	300	0.33	7.63

Note. By replacing the *G* for AGAL, the source name column (1) matches with the ATLASGAL simple names (Schuller et al. 2009; Urquhart et al. 2014, 2018). Column (4) presents the observed velocity dispersion, which was obtained by the fitting of the line profile of $C^{18}O$ ($J = 2 - 1$) averaged within the clump with a 1D Gaussian, which was observed by total power (TP). The distance from the Sun in column (5) is from Whitaker et al. (2017), and the dust temperature in column (6) is from Guzmán et al. (2015). Mass in column (7) is cited from Traficante et al. (2015), Contreras et al. (2017) for clumps in the first and fourth quadrants, respectively. Properties in columns (8), (9), (10), and (11) are fitting results of 2D Gaussian for 870 μm continuum images. International Celestial Reference System (ICRS).

(This table is available in machine-readable form.)

(s) at 70 μm, without checking for Spitzer point sources. We used the physical properties in Traficante et al. (2015) for the sample selection. We followed the same procedure for clumps designated as starless, and selected 20 prestellar, high-mass clump candidates (one presented in the pilot survey) that we visually inspected to verify a lack of emission from compact Spitzer sources. We finally included one 70 μm dark prestellar clump candidate, G023.477+00.114, that has a potential to form high-mass stars satisfying all conditions above that had been previously studied by Beuther et al. (2013, 2015). A detailed study of this source was presented using ASHES data in Morii et al. (2021). In summary, the entire ASHES sample is composed of 39 IRDC clumps (see Table 1).

Figure 1 shows the Spitzer and Herschel images for G010.991–00.082, one of the targets. The left panel shows the three-color composite image (3.6 μm in blue, 4.5 μm in green, and 8 μm in red) taken in the GLIMPSE survey (Benjamin et al. 2003). For comparison, the center and right panels display the 24 and 70 μm emission from the MIPSGAL (Carey et al. 2009) and Hi-GAL (Molinari et al. 2010) surveys, respectively, with contours of 870 μm continuum emission (Schuller et al. 2009).

2.2. Potential for High-mass Star Formation

Molecular cloud surveys suggest as empirical thresholds for high-mass star formation at a surface density >0.05 g cm^{-2}

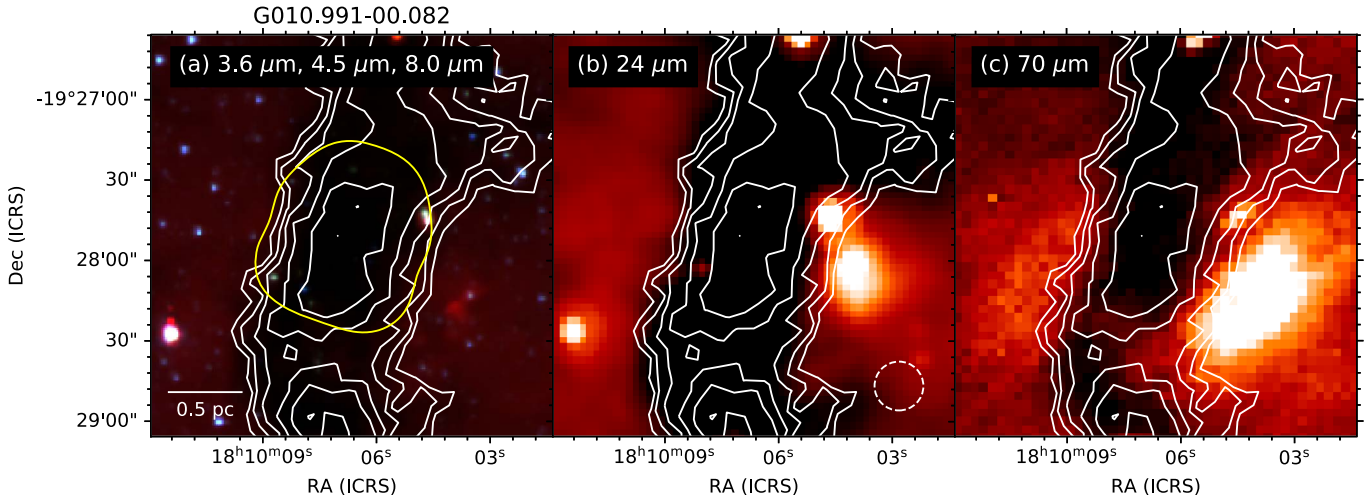

Figure 1. Spitzer and Herschel infrared images for G010.991–00.082. (a) Spitzer/IRAC three-color (3.6 μm in blue, 4.5 μm in green, and 8.0 μm in red) image. The yellow contour represents the area mosaicked with ALMA in ASHES. The white contours are 870 μm dust continuum emission from the ATLASGAL survey. Contour levels for the 870 μm dust continuum emission are (3, 4.2, 6, 8.5, 12, and 17)$\times\sigma$, where $\sigma = 71$ mJy beam^{-1} is the rms noise level. (b) Spitzer/MIPS 24 μm image, and (c) Herschel/PACS 70 μm image. A white dashed circle on the bottom right in panel (b) shows the beam size ($\sim$18.″2) of the ATLASGAL survey.

(The complete figure set of 39 images is available.)

(e.g., ATLASGAL Urquhart et al. 2014; He et al. 2015). Another threshold that has been proposed by Kauffmann & Pillai (2010), which after being scaled following Sanhueza et al. (2019), is $M > 580\,R^{1.33}$ (M and R are the mass and radius in units of $M_\odot$ and parsecs, respectively).

The mass and radius of clumps depend on the definition used in each study. Traficante et al. (2015) estimated the clump mass from the spectral energy distribution (SED) fitting of far-infrared wavelengths, while the radius of clumps is defined from the fitting of the 250 μm emission. In the MALT90 survey, Contreras et al. (2017) used the deconvolved radius from the 2D Gaussian fitting as the physical radius, and they estimated the clump mass from the radius and the column density, which was computed from SED fitting. Urquhart et al. (2018) estimated the clump mass using ATLASGAL 870 μm continuum emission. Additionally, the temperature and distances adopted are also different among catalogs.

The clump size is difficult to define because clumps are sometimes adjoining, and their borders are unclear. The definition and the measuring method are different from reference to reference. Typically, the clump mass is estimated from the column density obtained from SED fitting or from the ATLASGAL continuum flux with temperature information. One of the caveats for using the column density from the Herschel SED fitting is the low resolution of 35″ at 500 μm, which barely resolves clumps. Therefore, we decide to estimate the clump mass and radius using the ATLASGAL continuum emission, which has an angular resolution of 18.″2. We measured flux density (F_ν) and the radius of clumps ($R_{\rm cl}$) from a 2D Gaussian fitting of 870 μm ATLASGAL continuum images using CASA viewer (McMullin et al. 2007). The radius corresponds to half of the full width at half maximum of the best-fit Gaussian deconvolved with the beam size, estimated by using the CASA task `imfit`. Using the flux density of 870 μm continuum emission from the ATLASGAL survey, the clump mass can be estimated assuming optically thin conditions as follows:

$$M_{\rm cl} = \mathbb{R}\frac{d^2 F_\nu}{\kappa_\nu B_\nu(T_{\rm dust})}, \quad (1)$$

where $\mathbb{R} = 100$ is the gas-to-dust mass ratio, $\kappa_{0.87\ \rm mm} = 1.72\ {\rm cm^2\ g^{-1}}$ is the dust absorption coefficient, d is the distance to the source, and B_ν is the Planck function for a dust temperature $T_{\rm dust}$. The dust absorption coefficient ($\kappa_{0.87\ \rm mm}$) is calculated from $\kappa_{1.3\ \rm mm}$ assuming a dust emissivity spectral index (β) of 1.5, where $\kappa_{1.3\ \rm mm} = 0.9\ {\rm cm^2\ g^{-1}}$ is from Ossenkopf & Henning (1994; see Section 4.3). As for the dust temperature, we adopted the temperatures ($T_{\rm cl} \sim$ 10–20 K) from the SED fitting between 160 and 870 μm from Hi-GAL and ATLASGAL survey at the continuum peak position (Guzmán et al. 2015). We adopted the distances of clumps from Whitaker et al. (2017), ranging from 2.4 to 6 kpc. The different assumption that can be made on $\mathbb{R}$ is that it varies depending on the galactocentric distance. Comparing the variation of $\mathbb{R}$ with its uncertainties and with what is found in Sabatini et al. (2022), $\mathbb{R} = 100$ is a reasonable approximation. The uniformly recalculated clumps' properties, mass ($M_{\rm cl}$), radius ($R_{\rm cl}$), surface density ($\Sigma_{\rm cl} = M_{\rm cl}/(\pi R_{\rm cl}^2)$), and volume density ($n({\rm H_2})_{\rm cl} = M_{\rm cl}/\bar{m}_{\rm H_2}(4\pi R_{\rm cl}^3/3)$), are summarized in Table 1. Here, $\bar{m}_{\rm H_2}$ is the mean molecular mass per hydrogen molecule, and we adopt $\bar{m}_{\rm H_2} = 2.8\,m_{\rm H}$ (Kauffmann et al. 2008). Throughout this work, these are the clump properties that will be used in the analysis.

Figure 2 shows the mass as a function of clump radius colored by dust temperature. We overlaid the widely adopted thresholds for high-mass star formation as black lines. The solid one shows the high-mass star formation relation proposed by Kauffmann & Pillai (2010), as described above. The dashed line represents $\Sigma_{\rm cl} > 0.05\ {\rm g\ cm^{-2}}$ suggested by Urquhart et al. (2014), He et al. (2015). All targets from the ASHES sample

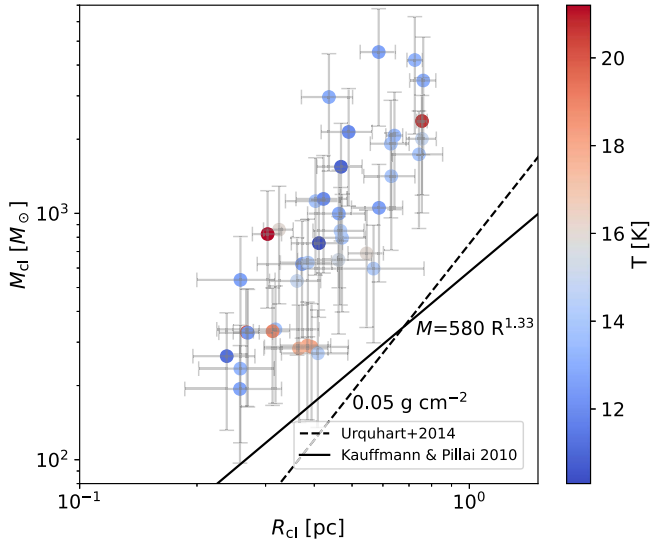

Figure 2. Mass–radius relation colored by dust temperature. Physical properties were derived from 2D Gaussian fitting to 870 μm continuum images. The black lines represent empirical thresholds for high-mass star formation ($M = 580\,R^{1.33}$). Dashed line corresponds to $\Sigma_{\rm cl} = 0.05$ g cm^{-2} (Urquhart et al. 2014). The relationship proposed by Kauffmann & Pillai (2010) is shown as a solid black line.

satisfy these thresholds and are therefore thought to be capable of forming high-mass stars.

Additionally, we can estimate a possible maximum stellar mass formed in a clump using the clump mass following Sanhueza et al. (2017, 2019). Larson (2003) obtained an empirical relation between the total stellar mass of a cluster ($M_{\rm cluster}$) and the maximum stellar mass in the cluster ($m^*_{\rm max}$) as

$$m^*_{\rm max} = 1.2\left(\frac{M_{\rm cluster}}{M_\odot}\right)^{0.45} M_\odot \quad (2)$$

$$= 15.6\left(\frac{M_{\rm clump}}{10^3\,M_\odot}\frac{\varepsilon_{\rm SFE}}{0.3}\right)^{0.45} M_\odot, \quad (3)$$

where the star formation efficiency ($\epsilon_{\rm SFE}$) is evaluated as $\varepsilon_{\rm SFE} = 0.1$–$0.3$ for nearby embedded clusters (Lada & Lada 2003). More recently, Sanhueza et al. (2019) derive another relation for the maximum stellar mass that could be formed in a clump following the Kroupa's initial mass function (Kroupa 2001) as

$$m^*_{\rm max} = \left(\frac{0.3}{\varepsilon_{\rm SFE}}\frac{21.0}{M_{\rm clump}/M_\odot} + 1.5\times10^{-3}\right)^{-0.77} M_\odot. \quad (4)$$

Here we assumed that the relation of $M_{\rm cluster} = \varepsilon_{\rm SFE} M_{\rm clump}$, with $M_{\rm clump} = M_{\rm cl}$ from Table 1. The calculated maximum stellar masses are in the range of $\sim$8–53 $M_\odot$, with an assumption of $\varepsilon_{\rm SFE} = 0.3$ for Equations (3) and (4).

Thus, the ASHES clumps fulfill known conditions for high-mass star formation, and they are therefore considered high-mass prestellar clump candidates in this work.

3. Observations and Data Reduction

Observations of the 39 ASHES clumps were carried out with ALMA in Band 6 ($\sim$224 GHz; $\sim$1.34 mm). The data were acquired through three cycles: Cycle 3 (2015.1.01539.S, PI: P. Sanhueza), Cycle 5 (2017.1.00716.S, PI: P. Sanhueza), and Cycle 6 (2018.1.00192.S, PI: P. Sanhueza). The observations were taken with the main 12 m array and the Atacama Compact Array including both the 7 m array and total power (TP). The whole IRDC clumps were covered by Nyquist-sampled ten-pointing and three-pointing mosaics with the 12 m array and the 7 m array, respectively. A ten-pointing mosaic corresponds to 0.97 arcmin^2 within the 20% power point, equivalent to the effective field of view (FOV) of $\sim1'$ per target. The mosaicked observations enable us to observe a large area of clumps as defined by single-dish continuum observations. The yellow contour in Figure 1 represents the FOV of the combined data (i.e., 12 + 7 m). The total on-source time of the 12 m array observations per mosaic was $\sim$16 minutes, while sources observed in multiple executions have a total time of $\sim$25 minutes per mosaic. As for the 7 m array observations, the total on-source time was $\sim$90–100 minutes for the first thirteen sources except for G023.477+00.114 ($\sim$30 minutes) and $\sim$50–70 minutes for the remaining sources in Table 2. Sources were observed in slightly different configurations through different ALMA cycles, resulting in slightly different angular resolutions. The observations are sensitive to structures with an angular scale smaller than $\sim11''$ and $\sim19''$ for 12 m array and 7 m array, respectively. The detailed observation setups and the synthesized beam sizes for all sources are summarized in Table 2.

Data reduction was carried out using CASA software package versions 4.5.3, 4.6, 4.7, and 5.4.0 for calibration and 5.4.0 and 5.6.0 for imaging (McMullin et al. 2007). Continuum images were produced by averaging line-free channels. The effective bandwidth for continuum emission was $\sim$3.7 GHz. After subtracting continuum emission, we combined the 12 m array data with the 7 m array data using the CASA task `concat`, and then the combined visibility data were Fourier transformed and cleaned together. In this work, we only used TP data of $C^{18}O$ ($J = 2-1$) line to estimate the velocity dispersion of the target clumps because TP antennas do not provide continuum emission.

All images have 512 × 512 pixels with a pixel size of $0\farcs2$. We used `TCLEAN` with Brigg's robust weighting of 0.5 to the visibilities and an imaging option of MULTISCALE with scales of 0, 5, 15, and 25 times the pixel size, considering the spatially extended nature of the emission in IRDCs. Average 1σ rms noise level is $\sim$0.094 mJy beam^{-1} with a beam size of $\sim1\farcs2$. The rms noise levels are also summarized in Table 2 for all targets. All images shown in this paper are the ALMA 12 and 7 m combined, before the primary beam correction, while all measured fluxes are derived from the combined data corrected for the primary beam attenuation.

4. Results

4.1. Dust Continuum Emission

The left panels of Figure 3 present the 1.3 mm continuum images for G010.991–00.082 and G014.492–00.139. We overlaid the single-dish 870 μm continuum emission obtained by ATLASGAL observations as black-dashed contours. Compared with the ATLASGAL observations, ALMA observations succeeded in resolving the area around the emission peak of massive clumps. As reported by the pilot survey (Sanhueza et al. 2019), we confirmed that the internal structures of these clumps vary from region to region: some are filamentary (e.g., G023.47 and G025.16), and some are clumpy

Table 2
Observational Parameters and Information for Continuum Images

Clump Name	Baselines (m)	Configuration	Number of Antennas	Beam Size ($''$ × $''$)	F_{12m+7m}/F_{12m}	F_{recov} (%)	rms Noise (mJy beam^{-1})
G010.991–00.082	15–330	C36–1	41 (9–10)	1.29 × 0.86	2.5	12	0.12
G014.492–00.139	15–330	C36–1	41 (9–10)	1.29 × 0.85	2.5	29	0.17
G015.203–00.441	15–314	C43–2	42–45 (9–12)	1.48 × 1.06	1.5	27	0.11
G016.974–00.222	15–314	C43–2	42–45 (9–12)	1.48 × 1.07	1.4	15	0.08
G018.801–00.297	15–314	C43–2	42–45 (9–12)	1.48 × 1.07	6.1	31	0.15
G018.931–00.029	15–314	C43–2	42–45 (9–12)	1.48 × 1.07	1.5	12	0.12
G022.253+00.032	15–314	C43–2	42–45 (9–12)	1.50 × 1.09	1.4	15	0.08
G022.692–00.452	15–314	C43–2	42–45 (9–12)	1.50 × 1.08	2.3	23	0.09
G023.477+00.114	15–314	C43–1	45 (10–11)	1.36 × 1.08	1.1	20	0.09
G024.010+00.489	15–314	C43–2	42–45 (9–12)	1.49 × 1.08	1.5	23	0.12
G024.524–00.139	15–314	C43–2	42–45 (9–12)	1.51 × 1.08	1.3	17	0.09
G025.163–00.304	15–314	C43–2	42–45 (9–12)	1.50 × 1.08	1.7	15	0.10
G028.273–00.167	15–314	C43–2	45–46 (10–12)	1.48 × 1.07	1.5	12	0.08
G028.541–00.237	15–314	C43–2	45–46 (10–12)	1.50 × 1.07	1.2	7	0.08
G028.564–00.236	15–314	C43–2	45–46 (10–12)	1.50 × 1.06	1.4	15	0.14
G028.927+00.394	15–314	C43–2	45–46 (10–12)	1.52 × 1.06	1.1	14	0.08
G030.704+00.104	15–314	C43–2	45–46 (10–12)	1.50 × 1.07	1.1	11	0.09
G030.913+00.719	15–314	C43–2	45–46 (10–12)	1.49 × 1.07	1.2	10	0.07
G033.331–00.531	15–314	C43–2	45–46 (10–12)	1.49 × 1.10	1.2	14	0.07
G034.133+00.076	15–314	C43–2	45–46 (10–12)	1.48 × 1.10	1.2	19	0.07
G034.169+00.089	15–314	C43–2	45–46 (10–12)	1.47 × 1.09	1.4	12	0.07
G034.739–00.119	15–314	C43–2	45–46 (10–12)	1.49 × 1.09	1.3	18	0.08
G036.666–00.114	15–314	C43–2	45–46 (10–12)	1.49 × 1.10	1.3	18	0.07
G305.794–00.096	15–455	C43–2	45 (10–11)	1.24 × 0.98	1.5	25	0.10
G327.116–00.294	15–330	C36–1	48(8)	1.32 × 1.11	1.3	17	0.09
G331.372–00.116	15–330	C36–1	48 (8)	1.34 × 1.09	1.8	21	0.08
G332.969–00.029	15–330	C36–1	48 (8)	1.35 × 1.08	1.7	11	0.08
G333.016–00.751	15–314	C43–2	46–48 (10–12)	1.49 × 1.11	1.6	11	0.08
G333.481–00.224	15–314	C43–2	46–48 (10–12)	1.48 × 1.11	1.6	20	0.08
G333.524–00.269	15–314	C43–2	46–48 (10–12)	1.49 × 1.10	1.5	17	0.12
G337.342–00.119	15–314	C43–2	46–48 (10–12)	1.43 × 1.10	1.4	7	0.07
G337.541–00.082	15–639	C36–2/3–C40-1	41–43 (8–9)	1.29 × 1.18	1.4	15	0.07
G340.179–00.242	15–704	C36–2/3–C40-4	36–41 (8–9)	1.41 × 1.29	2.7	9	0.09
G340.222–00.167	15–704	C36–2/3–C40-4	36–41 (8–9)	1.40 × 1.28	2.3	22	0.11
G340.232–00.146	15–704	C36–2/3–C40-4	36–41 (8–9)	1.39 × 1.26	3.9	45	0.14
G340.398–00.396	15–314	C43–2	46–48 (10–12)	1.41 × 1.09	1.5	10	0.08
G341.039–00.114	15–639	C36–2/3–C40-1	41–43 (8–9)	1.30 × 1.18	1.4	23	0.07
G343.489–00.416	15–639	C36–2/3–C40-1	41–43 (8–9)	1.30 × 1.18	1.5	15	0.07
G345.114–00.199	15–314	C43–2	46 (10–11)	1.25 × 1.12	2.0	12	0.08

Note. Baselines and configurations are observational setups for 12 m array. For 7 m array, the baselines range from 8 to 49 m. The number (or range) of antennas of 7 m is shown within parenthesis. When observations were carried out in the multiple execution blocks, and a different number of antennas were used, the variations were shown as ranges. The method to calculate the flux ratio and the recoverable fraction is described in Section 4.1. F_{recov} is recovered flux by ALMA with respect to single-dish observations. Continuum sensitivity and synthesized beam in the obtained 12 m+7 m combined images.

(This table is available in machine-readable form.)

(e.g., G014.49 and G333.52). We also resolved some clumps (e.g., G024.01 and G024.52) in networks of hub-filaments (see Section 5.2.4).

We combined the 12 m array and the 7 m array data to mitigate the missing flux. Indeed, the combined data have ∼1.7 times more flux than the 12 m only data for the entire FOV. To estimate how much flux is recovered in the combined images, we have scaled the 870 μm emission assuming a dust emissivity spectral index (β) of 1.5 as $F_{recov} = F_{1.3\,mm,ALMA}/F_{1.3\,mm,exp}$, where $F_{1.3\,mm,ALMA}$ is the 1.3 mm flux density obtained by ALMA in the FOV, and $F_{1.3\,mm,exp}$ is estimated as $F_{1.3\,mm,exp} = F_{0.87\,mm}(1.3/0.87)^{-(1.5+2)}$. $F_{0.87\,mm}$ was measured within the area corresponding to the ALMA FOV (blue contours in Figures 3). We integrated pixels where the intensity is more than twice the rms noise level to calculate $F_{1.3\,mm,\ ALMA}$. The estimated recoverable flux was between 7% and 45%. The estimated values (F_{12m+7m}/F_{12m} and F_{recov}) are summarized in Table 2. These are consistent with SMA and ALMA observations in other IRDC studies (e.g., Sanhueza et al. 2017; Liu et al. 2018).

4.2. Core Identification

We identified cores using the obtained 1.3 mm continuum images. In this paper, following the definitions of Sanhueza et al. (2019), we use the term "core" to describe a compact, dense object within a clump with a size of ∼0.01–0.1 pc, a mass of $\sim 10^{-1}$–10^{2} $M_{\odot}$, and a volume density of $\sim 10^{5}$ cm^{-3} that will likely form a single star or a small multiple system. We adopt the `dendrogram` technique (Rosolowsky et al. 2008) to extract cores, which is implemented in the

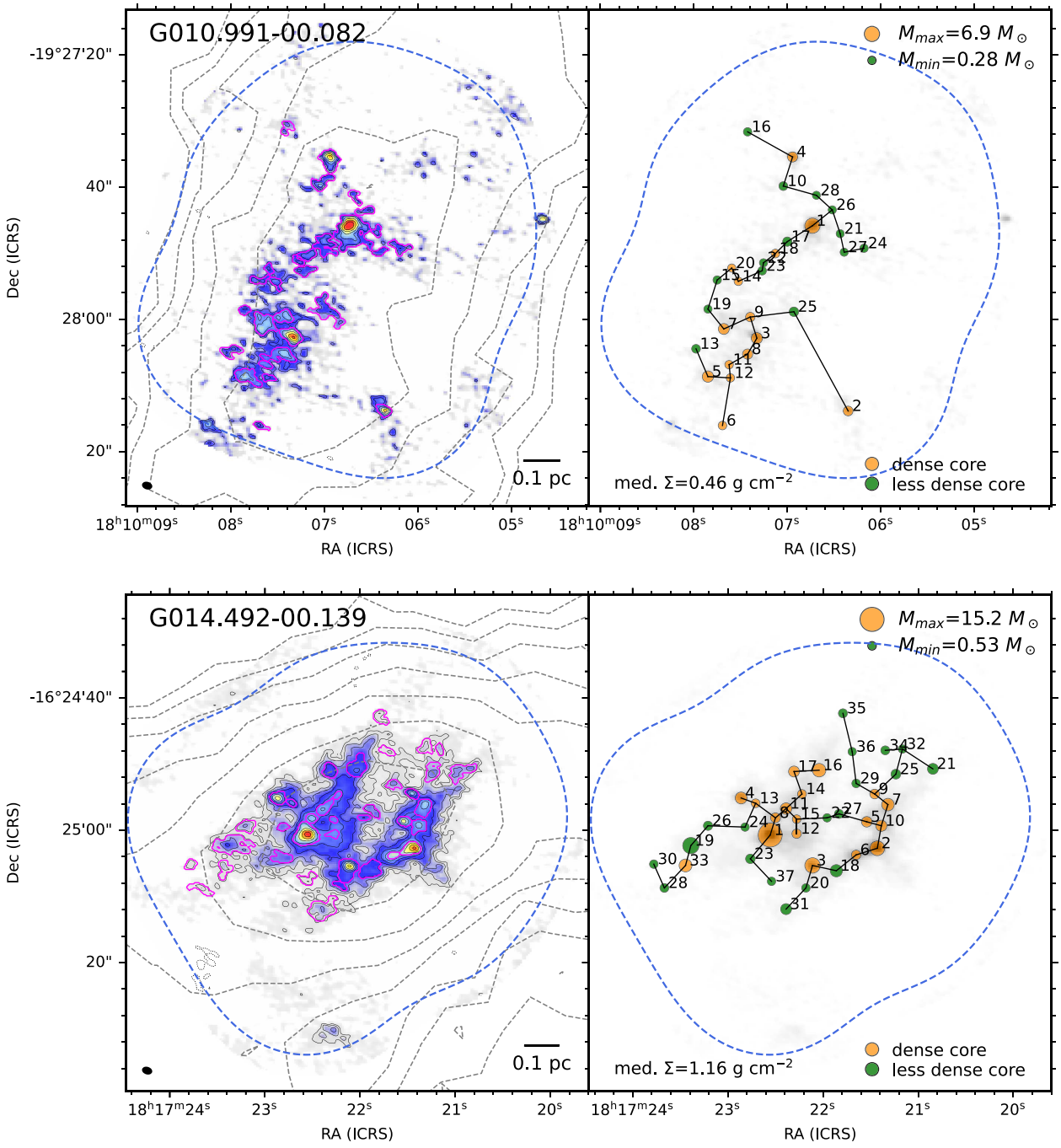

Figure 3. Left: ALMA 1.3 mm continuum image for two IRDCs, G010.991–00.82 and G014.492–00.139. Magenta thick contour represents leaf structures identified by the dendrogram algorithm (Section 4.2). Black-solid contours represent $3 \times 2^n\sigma$ (n = 1, 2, 3, ...), where σ is the continuum image rms noise levels summarized in Table 2. The dotted contours show the negative components (-4σ). The black-dashed contours show the 870 μm continuum emission from the ATLASGAL survey, which are the same as the white contours in Figure 1. The black ellipse in the bottom left corner represents the synthesized beam size. The black line indicates the spatial scale in the bottom right corner. The blue dashed contours correspond to a primary beam response of 30%. Right: circles represent core properties. The size corresponds to the estimated mass, and the position is centered at the continuum peak of each core. Orange circles represent cores with a surface density larger than the median of the cores' surface density of the corresponding clump, which are denoted on the bottom left (0.46 and 1.16 g cm^{-2} for G010.99 and G014.49, respectively). The remaining less dense cores are highlighted as green circles. Black segments show the outcome from the minimum spanning tree, which corresponds to the set of straight lines that connect cores in a way that minimizes the sum of the lengths. The digits represent the core ID named in order of peak intensity.

(The complete figure set of 39 images is available.)

Astrodendro Python package. The `dendrogram` technique classifies the hierarchical structure. The principal parameters are $F_{\rm min}$, δ, and $S_{\rm min}$. $F_{\rm min}$ sets the minimum value above which we define structures, and δ sets a minimum significance to separate them. $S_{\rm min}$ is the minimum number of pixels to be contained in the smallest individual structure (defined as a `leaf` in the `dendrogram` technique). The `dendrogram` algorithm classifies the hierarchical structures as `leaf`, `branch`, and `trunk`. A `leaf` is a structure that has no substructure, and a `trunk` is the largest structure. The remaining structure is `branch`, which has leaves as internal structures.

Table 3
Core Properties Obtained from Dendrogram

Clump Name	Core Name	R.A. (ICRS)	Decl. (ICRS)	$FWHM_{maj} \times FWHM_{min}$ ($''\times''$)	Peak Intensity (mJy beam^{-1})	Flux Density (mJy)
G010.991–00.082	ALMA1	18:10:06.73	− 19.27.45.85	2.81 × 2.59	2.70	12.63
G010.991–00.082	ALMA2	18:10:06.35	− 19.28.13.85	1.22 × 0.80	2.32	2.80
G010.991–00.082	ALMA3	18:10:07.32	− 19.28.02.85	1.78 × 1.12	2.27	4.91
G010.991–00.082	ALMA4	18:10:06.94	− 19.27.35.45	1.78 × 1.34	1.91	4.04
G010.991–00.082	ALMA5	18:10:07.85	− 19.28.08.65	2.41 × 1.15	1.41	4.33
G010.991–00.082	ALMA6	18:10:07.69	− 19.28.16.05	1.29 × 0.49	1.34	1.08
G010.991–00.082	ALMA7	18:10:07.68	− 19.28.01.45	1.95 × 1.69	1.09	4.60
G010.991–00.082	ALMA8	18:10:07.42	− 19.28.05.25	2.87 × 1.19	1.01	3.53
G010.991–00.082	ALMA9	18:10:07.39	− 19.27.59.65	1.67 × 1.00	0.88	2.12
G010.991–00.082	ALMA10	18:10:07.04	−19.27.39.85	2.12 × 1.01	0.86	1.60

(This table is available in its entirety in machine-readable form.)

Table 4
Core Physical Parameters

Clump Name	Core Name	T (K)	M_{core} ($M_\odot$)	$N_{peak}(H_2)$ ($\times10^{23}$ cm^{-2})	Radius (au)	Σ (g cm^{-2})	$n(H_2)$ ($\times10^6$ cm^{-3})
G010.991–00.082	ALMA1	13.4	6.90	1.62	4950	0.78	1.72
G010.991–00.082	ALMA2	12.5	1.68	1.53	1860	1.41	7.95
G010.991–00.082	ALMA3	12.1	3.10	1.57	2680	1.27	4.87
G010.991–00.082	ALMA4	14.1	2.05	1.06	2890	0.70	2.58
G010.991–00.082	ALMA5	10.8	3.24	1.16	3090	0.96	3.31
G010.991–00.082	ALMA6	13.2	0.60	0.82	1440	0.78	6.03
G010.991–00.082	ALMA7	12.2	2.87	0.75	3300	0.72	2.42
G010.991–00.082	ALMA8	12.3	2.17	0.68	3510	0.52	1.52
G010.991–00.082	ALMA9	11.5	1.44	0.66	2480	0.71	2.87
G010.991–00.082	ALMA10	12.8	0.92	0.55	2680	0.35	1.44

Note. T is the temperature used for mass calculation. The radius is calculated from the geometric mean of the FWHM divided by 2.
(This table is available in its entirety in machine-readable form.)

We set F_{min}, δ, and S_{min} as 2.5σ, 1.0σ, and the half-pixel numbers of the beam area following the pilot survey (Sanhueza et al. 2019). Since these parameters are optimistic values, we applied the additional constraint to the flux density to exclude suspicious structures. We have excluded the cores with a flux density smaller than 3.5σ. Additionally, we eliminated the cores at the edge of FOV. As a result of the `dendrogram` technique, 839 `leaf` structures were identified in total. The identified `leaf` structures are indicated as magenta contours in the left panels of Figure 3. We define a `leaf` as a core. The number of cores in each region ranges from 8 to 39 (median of 20). We named cores ALMA1, ALMA2, ... in order of the peak intensity. Table 3 gives peak position, size (major and minor FWHM), peak intensity, and flux density of cores identified by the dendrogram algorithm (the properties for all cores are summarized in a machine-readable table). As an example, the right panels in Figure 3 show the identified cores in G010.991–00.082 and G014.492–00.139 as circles. Each circle position corresponds to each core's continuum peak position, and the digits on the right panel show the core ID, indicating the order of the peak intensity in each region.

We confirmed only a weak correlation between the number of detected cores and the sensitivity, and between the number of detected cores and the clump distance with Spearman's rank coefficient of $r_s = -0.15$ and -0.22, and p–value is 0.36 and 0.17, respectively. Although the spatial resolution differs among the different clumps in the sample, this effect seems weak for the core identification.

4.3. Core Physical Parameters

Core masses can be estimated from the dust continuum emission, assuming the dust emission is optically thin, using Equation (1) following previous ASHES papers (Sanhueza et al. 2019; Morii et al. 2021). We adopt a gas-to-dust mass ratio of 100, and a dust opacity, $\kappa_{1.3\,mm} = 0.9$ cm^2 g^{-1} computed by Ossenkopf & Henning (1994) for the dust grains with the ice mantles at a volume density of 10^6 cm^{-3}. For the mass estimation, the fluxes obtained from dendrograms were used, without removing any additional background emission other than the inherently removed by the interferometer. In the case where the background emission is important, the core masses could be considered to be upper limits. For cores in eleven ASHES clumps, we used the rotational temperatures derived from NH_3 observations at $\sim5''$ (Li et al. 2022; D. Allingham et al. 2023, in preparation). For the remaining twenty-eight clumps, we adopted the clump temperature for the core mass calculation. Column (3) in Table 4 shows the temperature used for each core in the mass estimation. We confirmed that the dust emission is optically thin by using Equation (B.2) from Pouteau et al. (2022). We find that 99% of

cores have an optical depth smaller than 0.04, and the maximum value is ∼0.1.

The core mass ($M_{\rm core}$) given in column (4) of Table 4 ranges from 0.05 to 81 $M_\odot$. In the right panels in Figure 3, the size of circles indicates the core mass. More than half (∼55%) of the cores have a mass smaller than 1 $M_\odot$, and only 3.5% (29/839) of cores have $M_{\rm core} \gtrsim 10\,M_\odot$. Assuming a core-to-star formation efficiency (hereafter SFE) of 30%, ∼27 $M_\odot$ of core masses is necessary to form a high-mass star. In total, seven cores satisfy this mass threshold. Compared with the pilot survey, we revealed six additional high-mass cores thanks to the larger number of clumps. More discussion about core masses will be presented in Section 5.

By summing over the mass of all cores in each clump, we can estimate the core formation efficiency (CFE). We define the CFE as the ratio of the sum of core masses to the clump mass, $M_{\rm cl}$ (e.g., Louvet et al. 2014). It ranges from 0.6% to 16%, indicating that most of the clump mass has not been assembled into cores at the early phase traced in these 70 μm dark IRDCs. Table 5 summarize the core properties in each clump such as the total number of cores identified in each clump (N(core)), the maximum core mass ($M_{\rm max}$), the median of core mass ($M_{\rm med}$), and the minimum core mass ($M_{\rm min}$) as well as the CFE. Table 5 also shows $M_{3.5\sigma}$, the mass sensitivity in each clump, which corresponds to the mass when $F_{1.3\ {\rm mm}}$ is 3.5σ.

The major source of uncertainty in the mass calculation is the gas-to-dust mass ratio and the dust opacity. Assuming that all possible values of $\mathbb{R}$ and $\kappa_{1.3\ {\rm mm}}$ are distributed uniformly between the extreme values, $70 < \mathbb{R} < 150$ and $0.7 < \kappa_{1.3\ {\rm mm}} < 1.05$ (e.g., Devereux & Young 1990; Ossenkopf & Henning 1994; Vuong et al. 2003; Sabatini et al. 2019, 2022), the standard deviation can be estimated (Sanhueza et al. 2017). We adopt the uncertainties derived by Sanhueza et al. (2017) of 23% for the gas-to-dust mass ratio and 28% for the dust opacity, for the adopted values of 100 and 0.9 cm^2 g^{-1}, respectively. In addition, considering an absolute flux uncertainty of 10% for ALMA observations in Band 6, a temperature uncertainty of ∼20%, and a distance uncertainty of ∼10%, we estimate the uncertainties of core mass, volume density, and a surface density of ∼50% (see Sanhueza et al. 2017, 2019, for more details). For the protostellar cores, the actual dust temperature can be higher than the value derived at a coarser angular resolution using single-dish observations (Li et al. 2021; Morii et al. 2021). However, we confirm that the NH_3 kinetic temperatures derived at core scales in ASHES clumps with available NH_3 observations are lower than 23 K (Lu et al. 2015; Li et al. 2022). A similar range of NH_3 temperatures was also reported in other IRDC cores (Wang et al. 2014).

The core radius was defined as half of the geometric mean of the FWHM (Table 1) provided by Astrodendro; see additional details in the Astrodendro website.[16] The core radius ranges from $\sim 5 \times 10^{-3}$ to $\sim 5 \times 10^{-2}$ pc, corresponding to $\sim 10^3$–10^4 au, and its median is 2680 au. The core size is only $\lesssim$5% of the maximum recoverable scale, and the missing flux contribution for core mass estimation is expected to be small. The surface density, Σ, and the molecular volume density, $n(H_2)$, were estimated assuming a spherical core as follows: $\Sigma = M_{\rm core}/\pi r_{\rm core}^2$, and $n(H_2) = M_{\rm core}/\bar{m}_{H_2}(4\pi r_{\rm core}^3/3)$, where $r_{\rm core}$ is the core radius. Figure 4 shows the estimated radius and densities of cores. The orange lines are the cumulative histogram, indicating which percent of cores have higher density than a certain value. The estimated surface density ranges from ∼0.05 to 10 g cm^{-2}, and the volume density ranges from $\sim 10^5$ to 3×10^7 cm^{-3}. We found that ∼10% of cores (91/839) have a surface density higher than unity, which is the condition suggested by Krumholz & McKee (2008) as a threshold for high-mass star formation. They concluded that 1 g cm^{-2} is the minimum necessary to halt excessive fragmentation and allow formation of high-mass stars. Actually, all seven high-mass cores ($M_{\rm core} > 27\,M_\odot$) have a surface density higher than this threshold.

The peak column density, $N_{\rm peak}(H_2)$, was derived from

$$N_{\rm peak}(H_2) = \mathbb{R}\,\frac{I_{1.3\ {\rm mm,\ peak}}}{\Omega\,\bar{m}_{H_2}\,\kappa_{1.3\ {\rm mm}}\,B_{1.3\ {\rm mm}}(T_{\rm dust})}, \quad (5)$$

where $I_{1.3\ {\rm mm,\ peak}}$ is the peak intensity measured at the continuum peak, and Ω is the beam solid angle. In the top right

Table 5
Properties of Cores in Each Clump

Clump Name	N(core)[a]	$M_{\rm max}$ ($M_\odot$)	$M_{\rm med}$ ($M_\odot$)	$M_{\rm min}$ ($M_\odot$)	$M_{3.5\sigma}$ ($M_\odot$)	CFE[b] (%)
G010.991–00.082	28	6.9	0.67	0.28	0.26	1.5
G014.492–00.139	37	15.4	1.64	0.54	0.37	3.2
G015.203–00.441	26	5.2	0.30	0.06	0.05	5.3
G016.974–00.222	13	5.2	0.60	0.32	0.16	6.4
G018.801–00.297	8	10.0	2.78	1.25	0.46	0.7
G018.931–00.029	15	9.0	0.65	0.16	0.12	1.1
G022.253+00.032	16	6.2	1.14	0.32	0.29	8.3
G022.692–00.452	12	11.4	1.28	0.28	0.20	13.1
G023.477+00.114	19	22.6	1.44	0.41	0.34	6.7
G024.010+00.489	16	38.4	2.77	1.31	0.56	16.4
G024.524–00.139	23	13.1	1.74	0.53	0.41	1.7
G025.163–00.304	18	19.0	1.18	0.43	0.25	5.1
G028.273–00.167	19	8.4	2.78	0.67	0.39	3.5
G028.541–00.237	18	13.4	2.42	0.41	0.31	3.0
G028.564–00.236	35	81.1	3.83	0.75	0.58	6.7
G028.927+00.394	9	14.1	1.62	0.57	0.33	4.3
G030.704+00.104	21	15.7	1.02	0.44	0.35	2.3
G030.913+00.719	12	11.3	0.49	0.15	0.14	6.1
G033.331–00.531	9	28.9	0.61	0.38	0.34	6.1
G034.133+00.076	15	5.0	0.33	0.13	0.11	2.3
G034.169+00.089	22	1.7	0.25	0.11	0.10	2.6
G034.739–00.119	24	9.7	1.42	0.46	0.32	8.6
G036.666–00.114	13	10.4	0.55	0.19	0.13	9.8
G305.794–00.096	34	9.1	1.50	0.29	0.26	8.6
G327.116–00.294	21	10.8	0.51	0.11	0.17	5.0
G331.372–00.116	39	8.0	0.74	0.25	0.31	3.0
G332.969–00.029	20	4.1	0.47	0.26	0.22	1.5
G333.016–00.751	27	1.9	0.24	0.13	0.10	3.3
G333.481–00.224	25	6.7	0.42	0.12	0.09	8.3
G333.524–00.269	38	8.4	1.06	0.24	0.11	8.4
G337.342–00.119	16	2.6	0.56	0.22	0.20	4.2
G337.541–00.082	19	9.9	1.06	0.16	0.18	2.8
G340.179–00.242	16	1.9	0.63	0.16	0.21	0.6
G340.222–00.167	21	8.4	1.10	0.31	0.21	7.1
G340.232–00.146	16	31.7	1.06	0.37	0.27	6.2
G340.398–00.396	29	5.0	0.55	0.23	0.15	1.4
G341.039–00.114	35	7.3	0.60	0.13	0.11	5.5
G343.489–00.416	29	7.3	0.23	0.05	0.12	2.2
G345.114–00.199	26	2.1	0.37	0.13	0.12	4.4

Notes.
[a] Total number of cores identified in each clump.
[b] Core formation efficiency, a ratio of total core mass to clump mass.
(This table is available in machine-readable form.)

[16] https://dendrograms.readthedocs.io/en/stable/

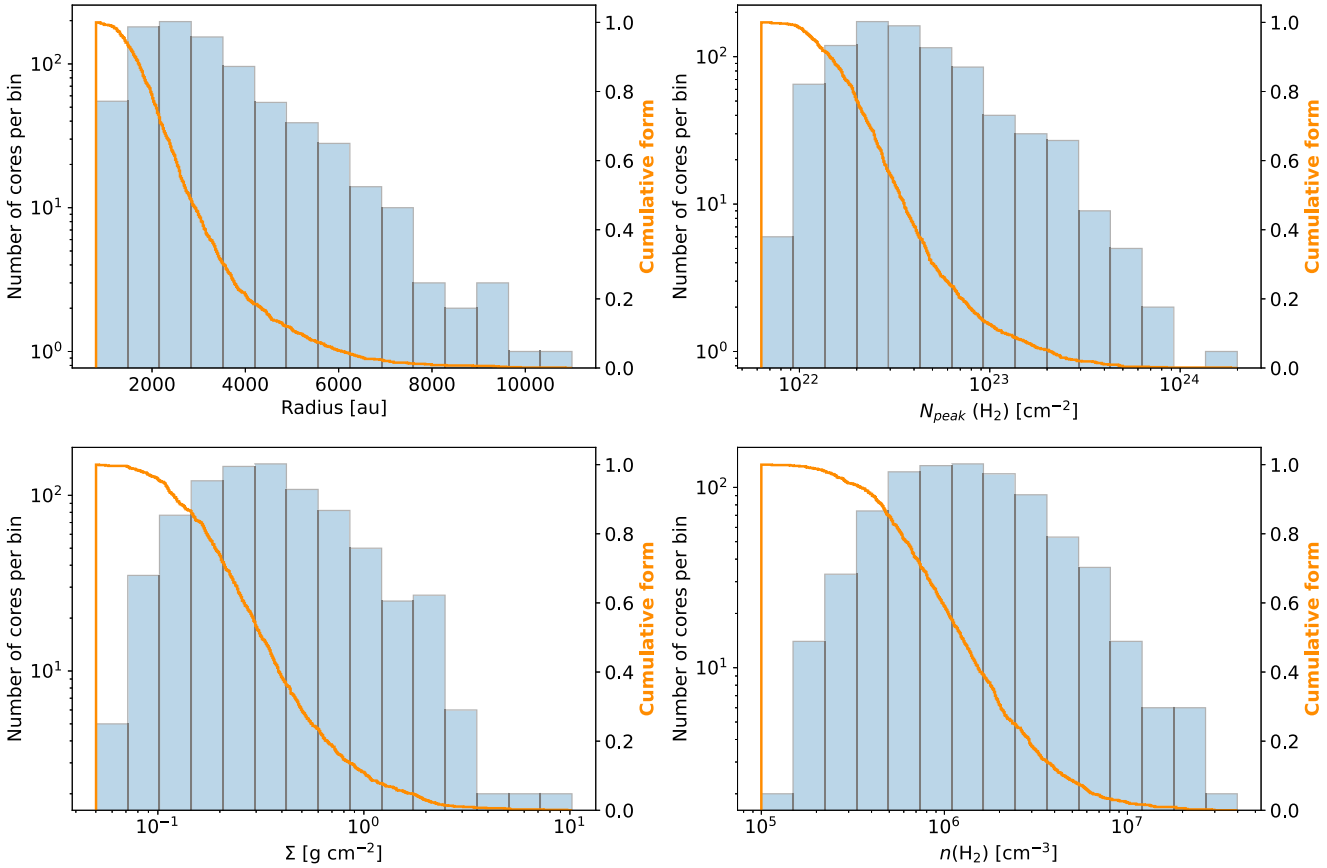

Figure 4. Core density properties such as core radius (astronomical units), peak column density ($N_{\rm peak}(H_2)$), surface density (Σ), and volume density ($n(H_2)$). Orange line in each panel represents the inverse-cumulative density distribution.

panel of Figure 4, the histogram of the peak column density is shown. It ranges from 10^{22} to 10^{24} cm^{-2} with a peak around 3×10^{22} cm^{-2}. The orange line indicates less than 20% of cores have a peak column density higher than 10^{23} cm^{-2}. The physical parameters of the cores are summarized in Table 4 (the full table can be accessed in machine-readable form).

4.4. Identification of Hub-filament System

In addition to the compact structures (cores), the continuum emission also resolved clumps in a network of filaments, some of which consist of hub-filament systems. A hub is the convergence of multiple filaments and recently caught more attention as the possible birthplace of high-mass stars (e.g., Motte et al. 2018).

We applied the publicly available filament finding package `FilFinder` (Koch & Rosolowsky 2015) to the ASHES continuum images to identify filamentary structures. It first creates a mask of a filamentary structure by adopting an intensity threshold, and each structure within the identified mask is reduced to a skeleton. These skeletonized structures are pruned by imposing thresholds for their lengths or sizes prior to obtaining the extracted filaments. We exclude very short structures and identified the prominent ones (see Appendix for more details).

Filamentary structures are identified in almost all clumps (36/39),[17] some of which contain hub-filament systems. The identified skeletons are highlighted as orange lines in Figure 5, for example. In this figure, the convergence point is a hub. We have identified 31 hubs in 17 ASHES clumps. We will discuss whether the MMCs or high-mass cores are preferentially located at such hub positions later (see Section 5.2). For this work, we focus on the dust continuum emission, and the detailed analysis of filaments and hubs is beyond the scope of this paper.

5. Discussion

5.1. Core Mass

The top panel of Figure 6 shows the core mass and the corresponding surface density of the natal clump. Red circles represent the MMCs in each clump, blue triangles represent mass sensitivity for each clump corresponding to the integrated intensity of 3.5σ. We find a moderate correlation between clump surface density and the maximum core mass with a Spearman's rank correlation coefficient of $r_s = 0.39$, and p–value $= 0.01$. The bottom panel of Figure 6 displays the differential core mass function (CMF) sharing the horizontal axis of the top panel. The core mass distribution peaks at around $0.6\,M_\odot$ (close to the worst mass sensitivity in the sample), and rapidly decreases toward the high-mass end. The detailed analysis for the CMF will be addressed in a dedicated paper under preparation (K. Morii et al. 2023, in preparation).

5.2. Most Massive Cores

As described in Section 2, at least one high-mass star is expected to be formed from each ASHES clump. In this

[17] Clumps in which no filamentary structure is identified are G018.801-00.297, G332.969-00.029, and G340.179-00.242.

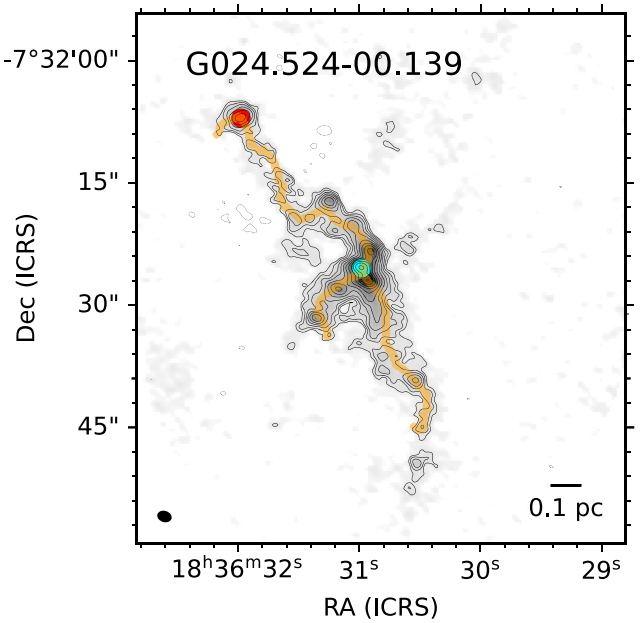

Figure 5. An example of identified filament in G025.524–00.139. Background image and contours are 1.3 mm continuum emission, the same as the right panel of Figure 3. Orange lines represent the identified skeleton by `FilFinder`. Red and cyan circles show the positions of the MMCs and second MMCs, respectively. Here, the circle size is constant (not representing core masses).

(The complete figure set of 3 images is available.)

section, we focus on the MMCs found in each clump (hereafter MMCs), those with $M_{\rm core} = M_{\rm max}$.

5.2.1. Correlation between the Maximum Core Mass and Clump Surface Density

In stellar clusters, higher-mass stars are found in higher-mass clusters (Larson 2003). In a similar fashion, it may be expected that higher-mass cores should form in higher-mass clumps. Here, to minimize the effect of having different spatial resolutions, we have limited the sample for this discussion. We have excluded the clumps that locate too close (<3.5 kpc) and too far (>5.5 kpc), and two more with the worst mass sensitivity ($>0.45 M_\odot$). As a result, the 30 clumps remaining are located between 3.5 and 5.5 kpc and have a mass sensitivity between 0.086 and 0.41 $M_\odot$. Figure 7 shows the scatter plots of the maximum core mass ($M_{\rm max}$) versus clump surface density, clump mass, distance, and clump surface density within a certain area. As seen in Figure 7, the clump surface density correlates with $M_{\rm max}$, having a Spearman's rank correlation coefficient $r_s = 0.55$, and p–value $= 0.0016$. On the other hand, $M_{\rm max}$ and clump mass weakly correlate with a Spearman's rank correlation coefficient of $r_s = 0.27$, and a p–value $= 0.15$. It indicates that the maximum core mass in each clump is not determined by the natal clump mass at least in the very early stages traced in the ASHES survey. Considering the relation between the cluster mass (clump mass) and the maximum stellar mass empirically derived by Larson (2003; see Equation (3) used earlier), the weak correlation implies the final stellar mass is not determined from the initial core mass. The left panel in Figure 7 would rather indicate that more massive cores form in clumps with higher surface density. We confirmed that the stronger correlation between the maximum

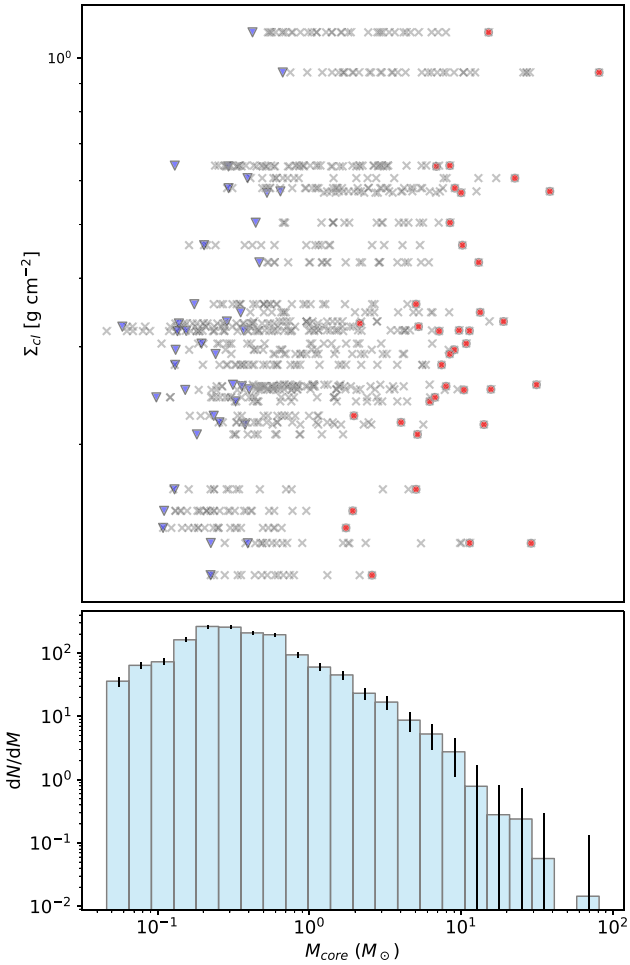

Figure 6. Top panel: clump surface density vs. core mass. Gray cross symbols correspond to all 839 cores. Red circles show the most massive cores in each clump. Blue triangles represent mass sensitivity for each clump corresponding to the integrated intensity of 3.5σ. Bottom panel: the core mass function of all 893 cores with uniform bin size in log-space. The errorbars represent the statistical error.

core mass and the clump surface density does not result from the codependence on the distance as shown in the right two panels of Figure 7. We recalculated the clump surface density within a circle with a radius of 0.45 pc centered on the mean positions of cores, ($\Sigma_{\rm cl,0.45\ pc}$) to reduce the dependence on distance. The circle almost corresponds to the FOV of the closest clump (3.5 kpc). A moderate correlation is present with a Spearman's rank correlation coefficient of $r_s = 0.43$, and p–value $= 0.017$.

5.2.2. The Lack of High-mass Prestellar Cores

We revealed 839 dense cores, among which about 55% are low-mass ($<1 M_\odot$). Although seven high-mass cores ($\gtrsim 27 M_\odot$) are identified thanks to a large sample, more than half of the ASHES clumps (23/39) host only cores with masses smaller than $10 M_\odot$. We compared the maximum core mass with the expected maximum stellar mass in Figure 8. Clumps are sorted in order of their masses, and the clump mass (and the expected maximum stellar mass) increases from left to right. The expected maximum stellar mass is estimated from the clump mass in two different ways, using Equations (3) and (4) (plotted as blue and green star symbols, respectively). We overplotted

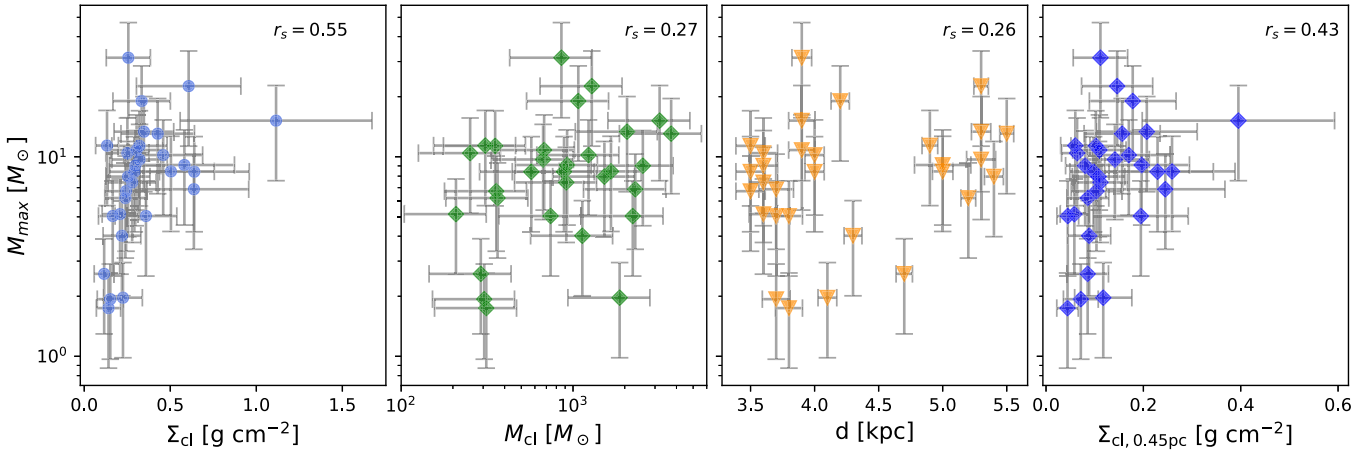

Figure 7. Maximum core mass (M_{max}) as a function of clump surface density (Σ_{cl}), clump mass (M_{cl}), distance (d), and $M_{cl,\,0.45\,pc}$ for selected 30 clumps. On the top left of each panel, Spearman's rank correlation coefficients are denoted.

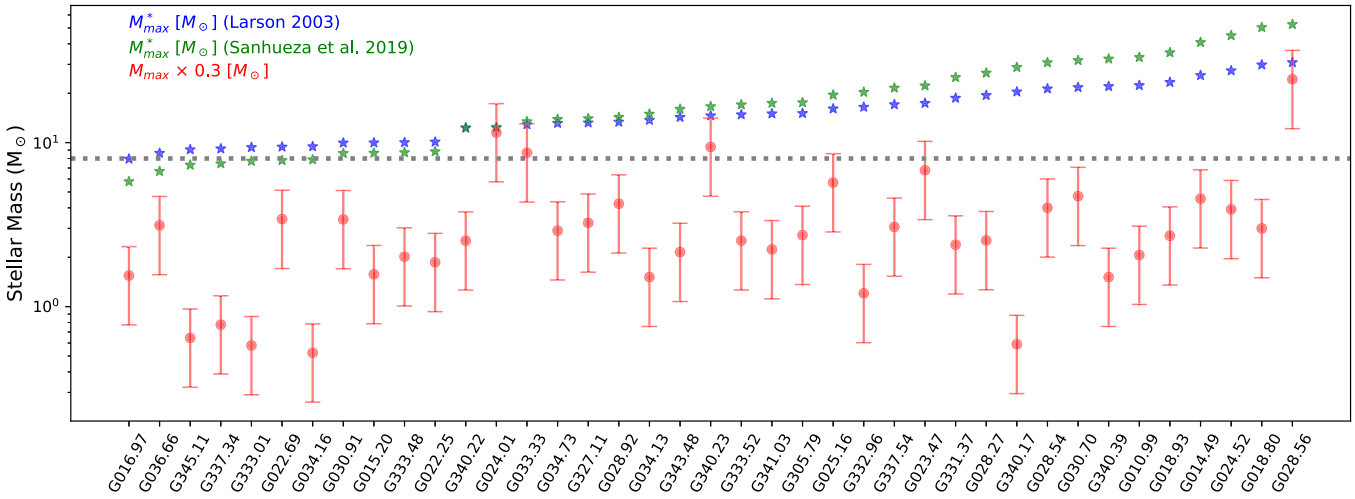

Figure 8. Comparison between stellar mass expected from clump mass and observed maximum core mass in each region. Blue and green star symbols correspond to the maximum stellar mass expected from their clump mass estimated from Equations (3) and (4) assuming $\varepsilon_{SFE} = 0.3$. Red circles are the maximum core mass in each region estimated in this work, multiplied by 0.3 to indicate the stellar mass with an assumption of SFE (from core to star) of 30%. Error bar shows the 50% uncertainty as mentioned in Section 4.3. The horizontal dotted line represents the stellar mass of 8 $M_\odot$. The plotting order in the horizontal axis is sorted by the clump mass.

M_{max} multiplied by 0.3 as red circles, assuming a core-to-star formation efficiency of 30%.

We again find no strong correlation between the maximum core mass and clump mass as mentioned in the previous section. Moreover, most red circles (30% of core mass) show lower masses than those of the blue and green stars (expected stellar masses). The majority of the ASHES clumps (35/39) have currently the MMCs with insufficient mass to form high-mass stars with the expected mass. This plot highlights that most cores in such a very early phase do not have sufficient mass to form high-mass stars without additional mass feeding, as predicted by clump-fed scenarios, such as competitive accretion, hierarchical collapse, and the inertial-inflow model. The MMCs in only four regions could form a high-mass star and have a mass near to the expected maximum stellar mass, assuming an SFE of 30% (G024.01, G028.56, G033.33, and G340.23). Even if we assume a higher SFE of 50%, only two additional clumps (G023.47 and G025.16) are added. We should note that these high-mass cores are associated with outflows traced by CO ($J = 2$–1) and also warm line emission such as H_2CO and CH_3OH ($E_u > 45$ K), implying that these high-mass cores present star formation signatures and are not prestellar (results that will be presented in a forthcoming paper).

The MMCs are generally intermediate-mass cores, more massive than the thermal Jeans mass of the host clump (e.g., 1–5 $M_\odot$). As an initial condition, the competitive accretion scenario predicts that clumps fragment into low-mass cores, comparable to the Jeans mass. It does not entirely match our observations in terms of core mass, although some of the maximum core masses may have been initially low-mass but have already grown by accreting gas from the surrounding medium. Contreras et al. (2018) estimated a core infall rate of $2 \times 10^{-3}\,M_\odot$ yr^{-1} in one core of the ASHES sample. Assuming that gas accretion with this infall rate continues for $\sim 2.0 \times 10^4$ yr, the mean freefall time of the 39 MMCs ($t_{ff} = \sqrt{3\pi/(32G\rho)}$), the cores can gain the additional mass of $\sim 40\,M_\odot$. Sabatini et al. (2021) estimated a duration of 5×10^4 yr for the 70 μm dark phase from 110 massive clumps at different evolutionary stages. This timescale, longer than the mean freefall time for the 39 more massive cores, suggests that the cores initially of a Jeans mass have sufficient time to accrete

and grow before becoming bright at IR wavelengths. In the following subsection, we will investigate whether MMCs are located at the position where efficient mass feeding is expected.

Using mosaic observations at high sensitivity, we have therefore revealed a large number of low-mass cores and the lack of high-mass prestellar cores, in dense, massive 70 μm dark clumps. Considering the large number of cores detected in this study (839 in 39 clumps), following Sanhueza et al. (2019), we can say with more confidence that high-mass prestellar cores do not exist, or, if they do, they should form later when environmental conditions are appropriate for their formation.

5.2.3. Weak Mass Segregation and Strong Density Segregation

Mass feeding scenarios, such as the competitive accretion model, expect high-mass cores to be formed from low-mass cores located near the bottom of the gravitational potential or (hub-)filaments where cores acquire mass more efficiently. The different spatial distribution of massive objects with respect to lower-mass objects is called mass segregation (e.g., Allison et al. 2009; Parker & Goodwin 2015). The segregation caused by two-body relaxation is called dynamical mass segregation (von Hoerner 1960; Meylan 2000), while the segregation found in young clusters, believed to be inherited from the initial fragmentation, is called primordial mass segregation (e.g., Alfaro & Román-Zúñiga 2018). The Herschel Gould Belt Survey (André et al. 2010) has found mass segregation in some star-forming region such as Aquila, Corona Australis, and W43-MM1 (Dib & Henning 2019), Orion A (Román-Zúñiga et al. 2019), Orion B (Parker 2018; Könyves et al. 2020), NGC6334 (Sadaghiani & Sánchez-Monge 2020), and NGC2264 (Nony et al. 2021) at ~0.01–0.1 pc scale. Dib & Henning (2019) indicates regions with more active star formation present centrally clustering core distributions and significant mass segregation. Our sample is expected to be in the very early phase of high-mass star and cluster formation without IR-bright sources and be the best target to investigate if there is primordial mass segregation in the very early phase.

Following the pilot survey (Sanhueza et al. 2019), we first studied mass segregation ratios (MSRs), $\Lambda_{\rm MSR}$ (Allison et al. 2009) and $\Gamma_{\rm MSR}$ (Olczak et al. 2011), based on the minimum spanning tree (MST) method developed by Barrow et al. (1985). MST connects cores (in this case), minimizing the sum of the length and determining a set of straight lines. Black line segments on the right panel in Figure 3 show an example of the outcome from MST. $\Lambda_{\rm MSR}$ compares the sum of the edge length of the MST ($l_{\rm MST}$) of random cores with that of the same number of massive cores:

$$\Lambda_{\rm MSR}(N_{\rm MST}) = \frac{\langle l_{\rm MST}^{\rm random}\rangle}{l_{\rm MST}^{\rm massive}} \pm \frac{\sigma_{\rm random}}{l_{\rm MST}^{\rm massive}}, \quad (6)$$

where $\langle l_{\rm MST}^{\rm random}\rangle$ is the sum of the edge length of $N_{\rm MST}$ random cores averaged by 1000 trial, and $l_{\rm MST}^{\rm massive}$ is that of $N_{\rm MST}$ MMCs. $\sigma_{\rm random}$ is the standard deviation associated with estimating the average value $\langle l_{\rm MST}^{\rm random}\rangle$. If massive cores are distributed similarly to random cores (i.e., no mass segregation), $\Lambda_{\rm MSR}$ would be close to unity. If massive cores are concentrated, and their distribution is different from the lower-mass cores (mass segregation), $\Lambda_{\rm MSR}$ becomes larger than unity. In turn, $\Lambda_{\rm MSR} < 1$ implies massive cores are spread out compared to others (inverse-mass segregation). We calculated $\Lambda_{\rm MSR}(N_{\rm MST})$ varying $N_{\rm MST}$ from two to the total number of cores in each clump, N(core). The second method ($\Gamma_{\rm MSR}$) uses the geometric mean of the edges ($\gamma_{\rm MST}$), not the sum of the edges ($l_{\rm MST}$)

$$\gamma_{\rm MST} = \left(\prod_{i=1}^{N({\rm core})-1} L_i\right)^{1/(N({\rm core})-1)}, \quad (7)$$

and defined by

$$\Gamma_{\rm MSR}(N_{\rm MST}) = \frac{\gamma_{\rm MST}^{\rm random}}{\gamma_{\rm MST}^{\rm massive}} (d\gamma_{\rm random})^{\pm 1}, \quad (8)$$

where $d\gamma_{\rm random}$ is the geometric standard deviation given by

$$d\gamma = \exp\left(\sqrt{\frac{\sum_{i=1}^{N({\rm core})-1}(\ln L_i - \ln \gamma_{\rm MST})^2}{N({\rm core}) - 1}}\right), \quad (9)$$

where L_i is the ith MST edge. The term $\gamma_{\rm MST}^{\rm random}$ is the geometric mean of the edges for $N_{\rm MST}$ random cores, and $\gamma_{\rm MST}^{\rm massive}$ is that for the $N_{\rm MST}$ massive cores. These two different MSRs ($\Lambda_{\rm MSR}$ and $\Gamma_{\rm MSR}$) are thought to behave in the same way, but Olczak et al. (2011) proposed that $\Gamma_{\rm MSR}$ is more sensitive to finding weak mass segregation.

Figure 9 shows the MSRs as $\Gamma_{\rm MSR}$ and $\Lambda_{\rm MSR}$ with changing $N_{\rm MST}$ from 2 to N(core). We display regions with relatively high MSR (max(MSR) > 2 at $N_{\rm MST} > 3$) or low MSR (max (MSR) < 0.5 at $N_{\rm MST} > 3$). For the remaining regions, $\Gamma_{\rm MSR}$ and $\Lambda_{\rm MSR}$ are consistent with unity (i.e., no mass segregation) for $N_{\rm MST} > 3$. The MSRs at $N_{\rm MST} = 3$ in six clumps is higher than 2, but MSRs' values gradually decrease for larger $N_{\rm MST}$ values. Only G034.73 shows a tentative detection of mass segregation with MSR of ~3 at $N_{\rm MST} = 5$. Compared with the pilot survey (Sanhueza et al. 2019), in which no evidence of mass segregation was found, this larger sample reveals weak detections of mass segregation in G018.80, G023.47, G024.01, G024.52, G028.92, and G034.73. We note that most of these clumps host no high-mass cores except for G024.01 ($M_{\rm max} = 38.4 M_\odot$), and there is no strong correlation between the maximum core mass and the MSR. Thus, the weak mass segregation found in the ASHES sample implies that the relatively high-mass cores (e.g., MMCs) form similarly to the lower-mass cores at the initial phase traced by the studied 70 μm dark IRDCs.

However, a caveat to keep in mind for this discussion is the small core sample used for estimating MSRs. Although the previous studies such as Dib & Henning (2019) treat about 100 objects, the sample here contains 40 at most.

If we replace $l_{\rm MST}^{\rm massive}$ in Equation (6) by $l_{\rm MST}^{\rm dense}$, an edge length of the $N_{\rm MST}$ densest cores instead of the MMCs, we can investigate whether denser cores are distributed differently from relatively less dense cores. We refer to this as density segregation. Figure 10 shows the segregation ratios $\Lambda(N_{\rm MST})$ calculated by sorting by core volume density, $n(\rm H_2)$ (top panels), and core surface density, Σ (bottom panels), instead of core mass. Using the same threshold as Figure 9, we only plot the clumps that show a high or low segregation ratio ($\Lambda > 2$ or <0.5, respectively). As the figures clearly show, contrary to mass segregation, the segregation by density was confirmed in about half of our sample, and their Λ values are generally higher than $\Lambda_{\rm MSR}$, implying a stronger segregation. We note that all six clumps with signs of mass segregation show density

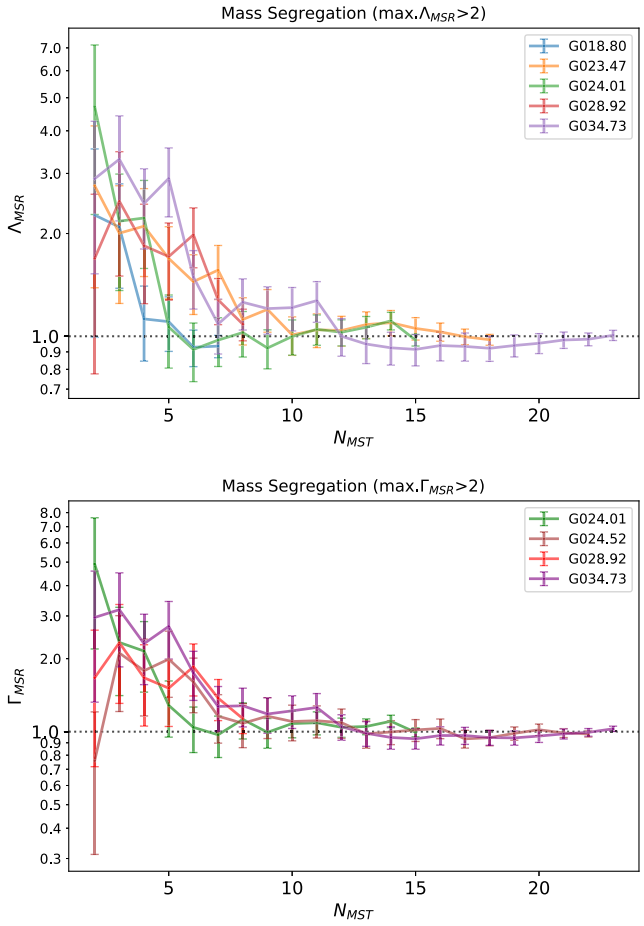

Figure 9. Mass segregation ratios values ($\Gamma_{\rm MSR}$ and $\Lambda_{\rm MSR}$) and the number of segments considered ($N_{\rm MST}$). Selected regions have relatively higher values, i.e., MSR values $\gtrsim$2 or low values (MSR<0.5) for $N_{\rm MST}=3$.

segregation as well. By carefully checking core positions, core masses, and densities, we found that mass segregation and density segregation occur around the same part within these clumps. To highlight the density segregation in Figure 3, we colored in orange the cores that are denser than the median of the surface density of all cores in the clump.

The density segregation may trace a segregation resulting from the different evolutionary stages of cores within a given clump. One may expect that cores become denser as they evolve. Thus, the density segregation observed may indicate that more evolved cores are segregated. Another possibility is that such denser cores are formed from the fragmentation of denser parts within clumps. We found a strong correlation between the clump surface density and the median of cores' surface density with a Spearman's rank correlation coefficient of $r_s=0.53$, and a p–value $=4.8\times10^{-4}$. Assuming that these correlations hold even at a smaller scale (i.e., within the clump), a denser region within a nonuniform clump would produce denser cores than a less dense part, resulting in density segregation. Therefore, the initial spatial distribution of cores would be dictated by density.

Alfaro & Román-Zúñiga (2018), Román-Zúñiga et al. (2019) also reported a spatial segregation by volume density stronger than the segregation by mass in the Pipe Nebula and Orion A. They concluded that density controls the clumpy spatial distribution of prestellar cores at the very early phase.

5.2.4. Spatial Distribution of MMCs: Hub-filament System

In addition to the weak mass segregation, we also found no significant difference in the spatial distribution between MMCs and the lower-mass cores. Since we have no information on the gravitational potentials of clumps, we assume that they are around the continuum peak of the single-dish observations. Figure 11 displays the plot of core mass versus separation from the continuum peak of each clump (hereafter clump peak position) obtained by single-dish observations (i.e., ATLASGAL survey). The MMCs in each clump are highlighted as orange, and the other cores are shown in blue circles. Above the worst mass sensitivity ($\sim$0.58 $M_\odot$), we cannot reject the null hypothesis at a 5% level that the separation distributions of MMCs (orange) and the other cores (blue) are identical since the estimated p–value is 0.47 from the Kolmogorov–Smirnov (KS) test. It implies that there is no significant difference. We note that this lack of difference in spatial distribution is confirmed when the clump peak positions are replaced with the mean position of cores identified by ALMA.

Alternatively, another preferred location for the MMCs could be a hub-filament system. Our observations resolve 70 μm dark massive clumps, revealing cores and filamentary structures within clumps. We revealed prominent hub-filament systems in some clumps, such as G024.524–00.139 and G025.163–00.304, as identified in Section 4.4. This motivates us to study whether there is correlation between the position of the MMCs and the hub-filament systems. Assuming that cores at hub positions can efficiently accumulate gas, more massive cores are expected to form at hub positions. We overlaid the MMCs and second MMCs as red and cyan circles, respectively, in Figure 5. Most of the MMCs are not located at such hub positions. Indeed, only eight (20%) MMCs are found at hubs. Even after considering the second MMC in each clump, only eleven cores in total are located in hubs ($11/(39\times2)=14\%$). Considering projection effects, the real percentage would be lower. If we focus on high-mass cores (>27 $M_\odot$), only a single clump hosts high-mass cores at hub positions among the 17 hub-hosting clumps. Our observations imply that the hub-filament systems within massive clumps at very early evolutionary stages are not yet efficiently contributing to core accretion. This is also in agreement with the finding that MMCs are similarly distributed to lower-mass cores at early stages, as we have discussed so far. Line emission, such as N_2H^+, would trace more extended emission, which may reveal more filaments or hub-filament systems.

However, half of the high-mass cores are located within filaments, implying that high-mass cores may form by acquiring gas along filaments, adding further support to previous studies (e.g., Henshaw et al. 2014; Peretto et al. 2014; Lu et al. 2018; Williams et al. 2018; Chen et al. 2019; Sanhueza et al. 2021; Zhou et al. 2022). Recently, Redaelli et al. (2022) revealed an accretion flow seen in N_2H^+ (J=1–0) in a target of the ASHES sample, G014.492-00.139, and estimated an accretion rate of 2×10^{-4} $M_\odot$ yr^{-1}. Assuming that this gas accretion feeds a core for its freefall time ($\sim2\times10^4$ yr), the core can acquire an additional mass of 4 $M_\odot$. There are an additional two MMCs in the whole 39 MMCs that can grow into high-mass cores ($\gtrsim$27 $M_\odot$) with this assumed accretion rate. However, we note that, with either a longer accretion time (e.g., $1.5\times t_{ff}$) or higher SFE (e.g., 50%), accretion through filaments would be substantial and key for the formation of high-mass stars. The study of gas dynamics

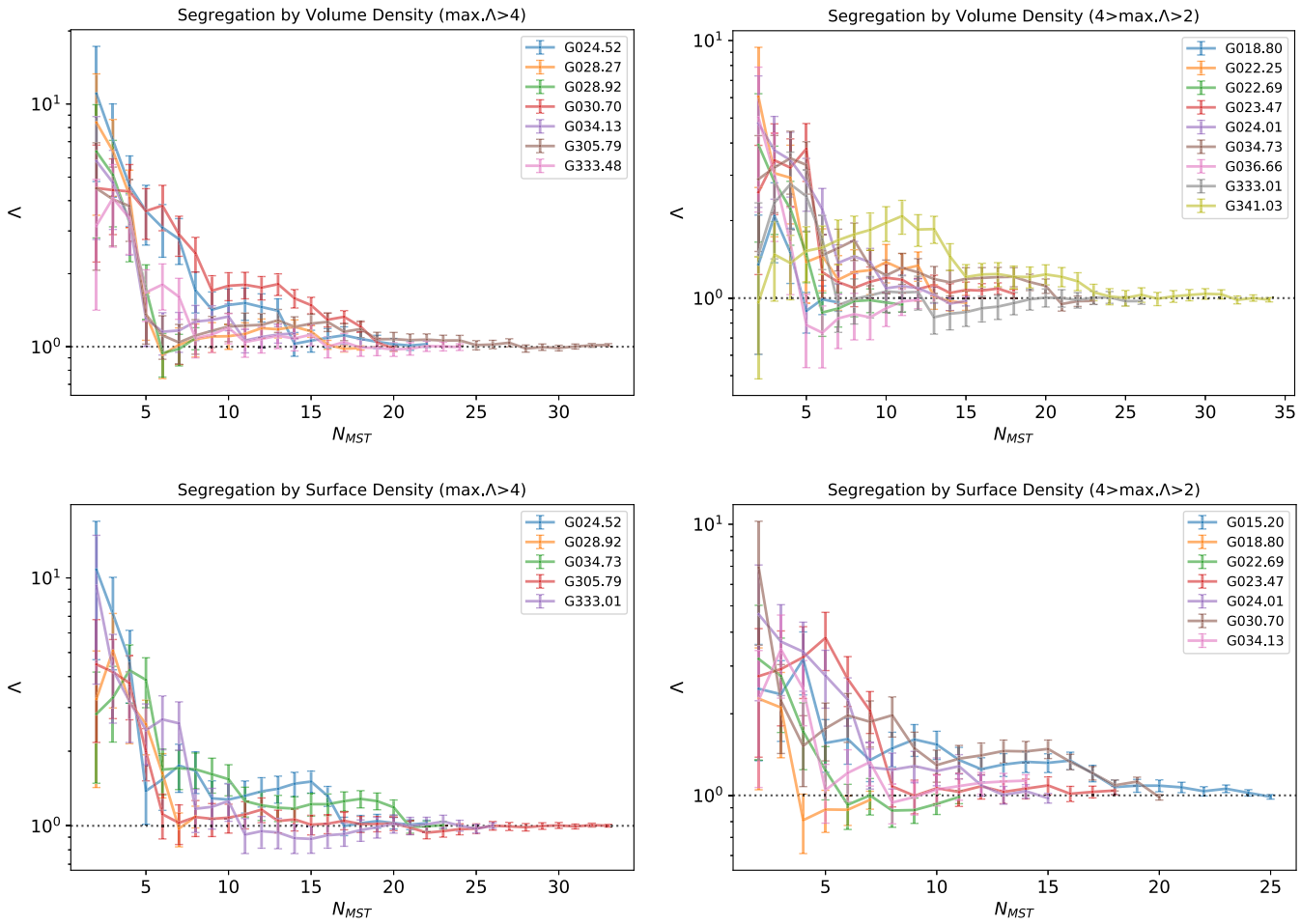

Figure 10. The segregation ratio Λ by volume density (top) and surface density (bottom). Selected regions have relatively higher values, i.e., $\Lambda > 4$ (left) or $4 > \Lambda > 2$ for (right) for $N_{\rm MST} = 3$.

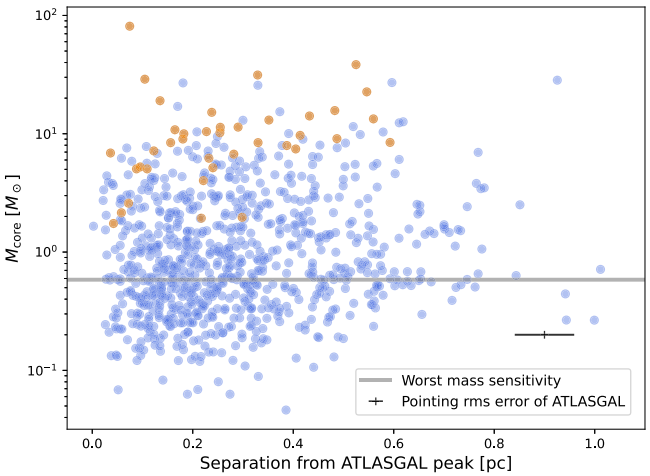

Figure 11. The distribution of core mass vs. separation from clump center. The clump center corresponds to the continuum peak obtained from single-dish observations (ATLASGAL survey). Circles represent all 839 cores, and the MMCs are highlighted in orange. There is no significant difference of separation between blue and orange circles, and it maintains even if the center is replaced with the mean position of cores in each clump.

around the whole population of ASHES cores would make clearer the role of accretion along filaments in the formation of high-mass stars.

5.3. Early Phase of High-mass Star Formation

Using ALMA observations toward 70 μm dark massive clumps, we have revealed the properties of hundreds of cores in the very early phases of high-mass star formation. The majority of the identified MMCs have insufficient mass to form high-mass stars following the core accretion scenario. In addition, no high-mass prestellar cores were detected. We only found a weak correlation between the maximum core mass and the natal clump mass, in contrast to the correlation between the maximum stellar mass and the cluster's mass (i.e., Larson's relation Equation (3)), implying that the initial core mass does not have to be correlated with the final stellar mass (e.g., Smith et al. 2009; Pelkonen et al. 2021). These conditions found in the ASHES sample support clump-fed accretion scenarios, such as competitive accretion, global hierarchical collapse, and the inertial-inflow model.

In spite of infall rate estimations being so far rare in IRDCs, the few examples available (Contreras et al. 2018; Chen et al. 2019; Redaelli et al. 2022) suggest that cores with masses as those found in ASHES cores can grow significantly in mass in a core freefall time (as discussed in two ASHES clumps; Contreras et al. 2018; Redaelli et al. 2022). Some ASHES cores have the conditions to become massive as hot cores and form high-mass stars. We note that we cannot completely rule out the core accretion picture. However, if high-mass prestellar cores exist, we constrain their formation to later times, once the

conditions for their formation may be adequate (e.g., a denser or warmer environment, or under the presence of a more turbulent medium or stronger magnetic field).

The high-resolution ALMA observations also reveal that 45% of the ASHES targets (18/39) have developed hub-filament systems. However, our analysis suggests that, at the moment, hub-filament systems do not efficiently contribute to the formation of high-mass stars (picture that can change at later evolutionary stages). As discussed in Section 5.2.4, only one clump (2.5%) hosts high-mass cores, and eight (20%) host their MMCs at a hub-position. Such low probability implies that the high-mass cores or the MMCs are not preferentially formed at hub-filament systems, but rather it implies that cores originally formed in hub-systems eventually evolved to become massive at later stages (Liu et al. (2023).

6. Conclusion

We have presented the whole ASHES (ALMA Survey of 70 μm dark High-mass clumps in Early Stages) survey that aims at characterizing the very early phase of high-mass star formation to constrain theoretical models. The sample consists of thirty-nine massive clumps, the central, denser regions of 70 μm dark IRDCs. We have conducted ALMA observations that resolve the whole clumps, mosaicked with ten and three pointing by the 12 and 7 m arrays, respectively, at a final angular resolution of $\sim 1\farcs2$. We have characterized the core physical properties and have analyzed them in conjunction with the clump properties using the dust continuum emission. We have obtained the following conclusions:

1. At $<10^4$ au scales, the dust continuum emission shows a diversity of morphologies in the thirty-nine clumps observed, presenting clumpy and filamentary structures, some of which host hub-filament systems.
2. Using the dendrograms algorithm applied to dust continuum emission, we identified cores from all thirty-nine clumps. The number of the identified cores in each clump ranges from 8 to 39 (median of 20); 839 in total.
3. We estimated core masses ranging from 0.05 $M_\odot$ to 81 $M_\odot$, with 2 orders of magnitude of dynamic range. More than half of the cores are low-mass with $M_{\rm core} < 1\ M_\odot$, and less than 1% of cores are high-mass ($M_{\rm core} > 27\ M_\odot$). The identified cores have a size of several times 10^3 au and a volume density of 10^5–10^7 cm^{-3}. About 10% of cores have surface densities of >1 g cm^{-2}.
4. The maximum core mass does not correlate with the clump mass; however, the clump surface density is moderately correlated with the maximum core mass.
5. Our observations revealed that 35 out of 39 clumps host no high-mass cores that can form high-mass stars at this juncture assuming an SFE of 30%. The lack of high-mass prestellar cores implies that high-mass cores do not exist, or they form later on in the clump evolution once conditions for their formation are met.
6. Using the identified core positions and the MST method, we found weak evidence of mass segregation. Instead, the cores are segregated by densities. Besides, there is no sign that the MMCs are preferentially located near the clump center or at hub-filament systems. These findings indicate that there is no preferred location for high-mass core formation in such an early phase.

Acknowledgments

K.M. is financially supported by Grants-in-Aid for the Japan Society for the Promotion of Science (JSPS) Fellows (KAKENHI Number JP22J21529), and also supported by FoPM, WINGS Program, the University of Tokyo. P.S. was partially supported by a Grant-in-Aid for Scientific Research (KAKENHI Number JP22H01271 and JP23H01221) of JSPS. H.B. acknowledges support from the DFG in the Collaborative Research Center SFB 881—project ID 138713538, "The Milky Way System" (subproject B1). G.G. acknowledges support by the ANID BASAL project FB210003. K.T. was supported by JSPS KAKENHI (Grant Number JP20H05645). This paper uses the following ALMA data: ADS/JAO.ALMA#2015.1.01539.S, ADS/JAO.ALMA#2017.1.00716.S, and ADS/JAO.ALMA#2018.1.00192.S ALMA is a partnership of ESO (representing its member states), NSF (USA) and NINS (Japan), together with NRC (Canada), MOST and ASIAA (Taiwan), and KASI (Republic of Korea), in cooperation with the Republic of Chile. The Joint ALMA Observatory is operated by ESO, AUI/NRAO, and NAOJ. Data analysis was in part carried out on the open-use data analysis computer system at the Astronomy Data Center (ADC) of the National Astronomical Observatory of Japan.

Facility: ALMA.

Software: CASA (v4.5.3, 4.6, 4.7, 5.4, 5.6; McMullin et al. 2007).

Appendix
Identification of Filaments

One method to identify filamentary structures is the publicly available filament finding package `FilFinder` (Koch & Rosolowsky 2015). Following the guideline, we first fit a log-normal distribution to the brightness data (continuum emission in our case) to identify the mean (μ) and standard deviation (σ) of the log-intensity, and flatten the image using an arctangent transform ($I' = I_0 \arctan(I/I_0)$), where the normalization is $I_0 \equiv \exp(\mu + 2\sigma)$. This aims to suppress significantly brighter objects than filamentary structures such as dense cores. Next, we smooth the flattened image with a Gaussian to minimize the variations within the filamentary structures. We create a mask of filamentary structure using the smoothed image. The width of the element used for the adaptive threshold mask is set by a parameter of `adapt thresh`. In this step, pixels, where the intensity is much greater than the medium of the neighborhood, are extracted. Additionally, the global threshold mask is combined as a final mask, which excludes the pixels below the noise level in the image. The parameters used for making masks are `smooth size` of 1.5 times beamwidth, `adapt thresh` of 2.5 times beamwidth, `glob thresh` of 2.5σ, and `size thresh` of 10 times the beam area, where σ is the rms noise level of each continuum image (input data), the beamwidth is the geometrical mean of the beam size (Table 2), and the beam area is the total pixel number in the synthesized beam. They are selected by checking outputs.

Structures within the mask are reduced to a skeleton using a medial axis transform. The algorithm drives the shortest path between each pair of endpoints and calculates the positions of the medial axis, a single-pixel width, for a skeleton. Thus, filamentary structures are identified as skeletons. The geometrical cleaning is applied to remove isolated nodes and very short components. We impose a lower length limit of 10 times the beamwidth for each skeleton, `nbeamlengths` in

FilFinder method, and 5 times the beamwidth for each branch (branchnbeamlengths). The pruning is tried 300 times in total. We adopted the same parameters for all regions. The extracted skeletons are drawn in Figure 5 as orange lines. It should be noted that output skeletons depend on the setting parameters, but the main conclusion is insensitive to them.

ORCID iDs

Kaho Morii https://orcid.org/0000-0002-6752-6061
Patricio Sanhueza https://orcid.org/0000-0002-7125-7685
Fumitaka Nakamura https://orcid.org/0000-0001-5431-2294
Qizhou Zhang https://orcid.org/0000-0003-2384-6589
Giovanni Sabatini https://orcid.org/0000-0002-6428-9806
Henrik Beuther https://orcid.org/0000-0002-1700-090X
Xing Lu https://orcid.org/0000-0003-2619-9305
Shanghuo Li https://orcid.org/0000-0003-1275-5251
Guido Garay https://orcid.org/0000-0003-1649-7958
James M. Jackson https://orcid.org/0000-0002-3466-6164
Fernando A. Olguin https://orcid.org/0000-0002-8250-6827
Daniel Tafoya https://orcid.org/0000-0002-2149-2660
Ken'ichi Tatematsu https://orcid.org/0000-0002-8149-8546
Natsuko Izumi https://orcid.org/0000-0003-1604-9127
Takeshi Sakai https://orcid.org/0000-0003-4521-7492
Andrea Silva https://orcid.org/0000-0001-9500-604X

References

Aguirre, J. E., Ginsburg, A. G., Dunham, M. K., et al. 2011, ApJS, 192, 4
Alfaro, E. J., & Román-Zúñiga, C. G. 2018, MNRAS Lett., 478, L110
Allison, R. J., Goodwin, S. P., Parker, R. J., et al. 2009, MNRAS, 395, 1449
André, P., Men'shchikov, A., Bontemps, S., et al. 2010, A&A, 518, L102
Barnes, A. T., Henshaw, J. D., Fontani, F., et al. 2021, MNRAS, 503, 4601
Barrow, J. D., Bhavsar, S. P., & Sonoda, D. H. 1985, MNRAS, 216, 17
Benjamin, R. A., Churchwell, E., Babler, B. L., et al. 2003, PASP, 115, 953
Beuther, H., Henning, T., Linz, H., et al. 2015, A&A, 581, A119
Beuther, H., Linz, H., Tackenberg, J., et al. 2013, A&A, 553, A115
Bonnell, I. A., Bate, M. R., Clarke, C. J., & Pringle, J. E. 2001, MNRAS, 323, 785
Bonnell, I. A., Vine, S. G., & Bate, M. R. 2004, MNRAS, 349, 735
Carey, S. J., Noriega-Crespo, A., Mizuno, D. R., et al. 2009, PASP, 121, 76
Chambers, E. T., Jackson, J. M., Rathborne, J. M., & Simon, R. 2009, ApJS, 181, 360
Chen, H.-R. V., Zhang, Q., Wright, M. C. H., et al. 2019, ApJ, 875, 24
Contreras, Y., Rathborne, J. M., Guzman, A., et al. 2017, MNRAS, 466, 340
Contreras, Y., Sanhueza, P., Jackson, J. M., et al. 2018, ApJ, 861, 14
Csengeri, T., Bontemps, S., Wyrowski, F., et al. 2017, A&A, 600, L10
Devereux, N. A., & Young, J. S. 1990, ApJ, 359, 42
Dib, S., & Henning, T. 2019, A&A, 629, A135
Feng, S., Li, D., Caselli, P., et al. 2020, ApJ, 901, 145
Foster, J., Rathborne, J., Jackson, J., et al. 2013, in ASP Conf. Ser. 476, New Trends in Radio Astronomy in the ALMA Era: The 30th Anniversary of Nobeyama Radio Observatory, ed. R. Kawabe, N. Kuno, & S. Yamamoto (San Francisco, CA: ASP), 127
Foster, J. B., Jackson, J. M., Barnes, P. J., et al. 2011, ApJS, 197, 25
Guzmán, A. E., Sanhueza, P., Contreras, Y., et al. 2015, ApJ, 815, 130
He, Y.-X., Zhou, J.-J., Esimbek, J., et al. 2015, MNRAS, 450, 1926
Henshaw, J. D., Caselli, P., Fontani, F., Jiménez-Serra, I., & Tan, J. C. 2014, MNRAS, 440, 2860
Hogge, T., Jackson, J., Stephens, I., et al. 2018, ApJS, 237, 27
Jackson, J. M., Rathborne, J. M., Foster, J. B., et al. 2013, PASA, 30, e057
Jackson, J. M., Rathborne, J. M., Shah, R. Y., et al. 2006, ApJS, 163, 145
Kauffmann, J., Bertoldi, F., Bourke, T. L., Evans, N. J. I., & Lee, C. W 2008, A&A, 487, 993
Kauffmann, J., & Pillai, T. 2010, ApJL, 723, L7
Kirk, H., Johnstone, D., & Di Francesco, J. 2006, ApJ, 646, 1009
Koch, E. W., & Rosolowsky, E. W. 2015, MNRAS, 452, 3435
Könyves, V., André, P., Arzoumanian, D., et al. 2020, A&A, 635, A34
Kroupa, P. 2001, MNRAS, 322, 231
Krumholz, M. R., & McKee, C. F. 2008, Natur, 451, 1082
Kumar, M. S. N., Palmeirim, P., Arzoumanian, D., & Inutsuka, S. I. 2020, A&A, 642, A87
Lada, C. J., & Lada, E. A. 2003, ARA&A, 41, 57
Larson, R. B. 2003, in ASP Conf. Ser. 287, Galactic Star Formation Across the Stellar Mass Spectrum, ed. J. M. De Buizer & N. S. van der Bliek (San Francisco, CA: ASP), 65
Li, S., Lu, X., & Zhang, Q. 2021, ApJL, 912, L7
Li, S., Sanhueza, P., Lu, X., et al. 2022, ApJ, 939, 102
Li, S., Sanhueza, P., Zhang, Q., et al. 2023, ApJ, 949, 109
Li, S., Sanhueza, P., Zhang, Q., et al. 2020, ApJ, 903, 119
Li, S., Zhang, Q., Pillai, T., et al. 2019, ApJ, 886, 130
Liu, H.-L., Sanhueza, P., Liu, T., et al. 2020, ApJ, 901, 31
Liu, H.-L., Tej, A., Liu, T., et al. 2022, MNRAS, 510, 5009
Liu, H.-L., Tej, A., Liu, T., et al. 2023, MNRAS, 522, 3719
Liu, M., Tan, J. C., Cheng, Y., & Kong, S. 2018, ApJ, 862, 105
Louvet, F., Motte, F., Hennebelle, P., et al. 2014, A&A, 570, A15
Louvet, F., Neupane, S., Garay, G., et al. 2019, A&A, 622, A99
Lu, X., Zhang, Q., Liu, H. B., et al. 2018, ApJ, 855, 9
Lu, X., Zhang, Q., Wang, K., & Gu, Q. 2015, ApJ, 805, 171
McKee, C. F., & Tan, J. C. 2002, Natur, 416, 59
McKee, C. F., & Tan, J. C. 2003, ApJ, 585, 850
McMullin, J. P., Waters, B., Schiebel, D., Young, W., & Golap, K. 2007, in ASP Conf. Ser. 376, Astronomical Data Analysis Software and Systems XVI, ed. R. A. Shaw, F. Hill, & D. J. Bell (San Francisco, CA: ASP), 127
Meylan, G. 2000, in ASP Conf Ser. 211, Massive Stellar Clusters, ed. A. Lançon & C. M. Boily (San Francisco, CA: ASP), 215
Molinari, S., Swinyard, B., Bally, J., et al. 2010, A&A, 518, L100
Morii, K., Sanhueza, P., Nakamura, F., et al. 2021, ApJ, 923, 147
Motte, F., Bontemps, S., & Louvet, F. 2018, ARA&A, 56, 41
Myers, P. C. 2009, ApJ, 700, 1609
Nony, T., Robitaille, J. F., Motte, F., et al. 2021, A&A, 645, A94
Ohashi, S., Sanhueza, P., Chen, H.-R. V., et al. 2016, ApJ, 833, 209
Olczak, C., Spurzem, R., & Henning, T. 2011, A&A, 532, A119
Olguin, F. A., Sanhueza, P., Guzmán, A. E., et al. 2021, ApJ, 909, 199
Ossenkopf, V., & Henning, T. 1994, A&A, 291, 943
Padoan, P., Pan, L., Juvela, M., Haugbølle, T., & Nordlund, Å. 2020, ApJ, 900, 82
Parker, R. J. 2018, MNRAS, 476, 617
Parker, R. J., & Goodwin, S. P. 2015, MNRAS, 449, 3381
Pelkonen, V.-M., Padoan, P., Haugbølle, T., & Nordlund, Å. 2021, MNRAS, 504, 1219
Peretto, N., Fuller, G. A., André, P., et al. 2014, A&A, 561, A83
Pillai, T., Kauffmann, J., Zhang, Q., et al. 2019, A&A, 622, A54
Pouteau, Y., Motte, F., Nony, T., et al. 2022, A&A, 664, A26
Rathborne, J. M., Jackson, J. M., & Simon, R. 2006, ApJ, 641, 389
Redaelli, E., Bovino, S., Sanhueza, P., et al. 2022, ApJ, 936, 169
Román-Zúñiga, C. G., Alfaro, E., Palau, A., et al. 2019, MNRAS, 489, 4429
Rosolowsky, E. W., Pineda, J. E., Kauffmann, J., & Goodman, A. A. 2008, ApJ, 679, 1338
Sabatini, G., Bovino, S., Giannetti, A., et al. 2021, A&A, 652, A71
Sabatini, G., Bovino, S., Sanhueza, P., et al. 2022, ApJ, 936, 80
Sabatini, G., Giannetti, A., Bovino, S., et al. 2019, MNRAS, 490, 4489
Sadaghiani, M., Sánchez-Monge, Á., Schilke, P., et al. 2020, A&A, 635, A2
Sakai, T., Sakai, N., Furuya, K., et al. 2015, ApJ, 803, 70
Sakai, T., Sanhueza, P., Furuya, K., et al. 2022, ApJ, 925, 144
Sakai, T., Yanagida, T., Furuya, K., et al. 2018, ApJ, 857, 35
Sanhueza, P., Contreras, Y., Wu, B., et al. 2019, ApJ, 886, 102
Sanhueza, P., Girart, J. M., Padovani, M., et al. 2021, ApJL, 915, L10
Sanhueza, P., Jackson, J. M., Foster, J. B., et al. 2012, ApJ, 756, 60
Sanhueza, P., Jackson, J. M., Foster, J. B., et al. 2013, ApJ, 773, 123
Sanhueza, P., Jackson, J. M., Zhang, Q., et al. 2017, ApJ, 841, 97
Schneider, N., Csengeri, T., Bontemps, S., et al. 2010, A&A, 520, A49
Schuller, F., Menten, K. M., Contreras, Y., et al. 2009, A&A, 504, 415
Smith, R. J., Longmore, S., & Bonnell, I. 2009, MNRAS, 400, 1775
Svoboda, B. E., Shirley, Y. L., Traficante, A., et al. 2019, ApJ, 886, 36
Tafoya, D., Sanhueza, P., Zhang, Q., et al. 2021, ApJ, 913, 131
Tan, J. C., Beltrán, M. T., Caselli, P., et al. 2014, in Protostars and Planets VI, ed. H. Beuther et al. (Tucson, AZ: Univ. Arizona Press), 149
Traficante, A., Fuller, G. A., Peretto, N., Pineda, J. E., & Molinari, S. 2015, MNRAS, 451, 3089
Urquhart, J. S., König, C., Giannetti, A., et al. 2018, MNRAS, 473, 1059
Urquhart, J. S., Moore, T. J. T., Csengeri, T., et al. 2014, MNRAS, 443, 1555
Vázquez-Semadeni, E., Palau, A., Ballesteros-Paredes, J., Gómez, G. C., & Zamora-Avilés, M. 2019, MNRAS, 490, 3061
von Hoerner, S. 1960, ZA, 50, 184
Vuong, M. H., Montmerle, T., Grosso, N., et al. 2003, A&A, 408, 581

Wang, K., Zhang, Q., Testi, L., et al. 2014, MNRAS, 439, 3275
Wang, K., Zhang, Q., Wu, Y., & Zhang, H. 2011, ApJ, 735, 64
Wang, P., Li, Z.-Y., Abel, T., & Nakamura, F. 2010, ApJ, 709, 27
Whitaker, J. S., Jackson, J. M., Rathborne, J. M., et al. 2017, AJ, 154, 140
Williams, G. M., Peretto, N., Avison, A., Duarte-Cabral, A., & Fuller, G. A. 2018, A&A, 613, A11
Zhang, Q., Qiu, K., Girart, J. M., et al. 2014, ApJ, 792, 116
Zhang, Q., & Wang, K. 2011, ApJ, 733, 26
Zhang, Q., Wang, K., Lu, X., & Jiménez-Serra, I. 2015, ApJ, 804, 141
Zhang, Q., Wang, Y., Pillai, T., & Rathborne, J. 2009, ApJ, 696, 268
Zhang, S., Zavagno, A., López-Sepulcre, A., et al. 2021, A&A, 646 A25
Zhou, J.-W., Liu, T., Evans, N. J., et al. 2022, MNRAS, 514, 6038